Dynamic characterisation and modelling of a slew drive system of offshore cranes

by

T.A. van Vugt

to obtain the degree of Master of Science
at the Delft University of Technology,
to be defended publicly on Thursday October 22, 2020 at 11:00 AM.

Student number:	4481925	
Project duration:	Novermber 11, 2019 – October 22, 2020	
Thesis committee:	Dr. Ir. H. Polinder,	TU Delft, supervisor
	Dr. Ir. S.A. Miedema,	TU Delft, chair
	Dr. Ir. X. Jiang,	TU Delft
	Dr. Ir. A. Nuttall,	Huisman Equipment

An electronic version of this thesis is available at http://repository.tudelft.nl/.

TU Delft

Acknowledgement

This thesis would not have been possible without the help of various people, whom I would like to acknowledge.

I would like to start with the company I did my graduation at, Huisman Equipment. I want to thank you for giving me the opportunity to work on this project. Secondly, I want to thank my daily supervisor of the TU Delft, Henk Polinder, for the guidance and information during my graduation. Thirdly, I want to thank my supervisor from Huisman, Ashley Nuttall, to provide me with much inside regarding the design of offshore cranes and its practical side and to help me get acquainted with the company. Fourthly, I would like to thank Sape Miedema for being my chair and giving me feedback during my intermediate presentations. I would also like to thank Xiaoli Jiang for being part of the committee and to connect me with Huisman. Furthermore, I would like to thank all the colleagues at Huisman to help me and make me feel welcome. Last, but certainly not least, I would like to show my thanks to my family, friends, and partner for their mental support and encouragement during this thesis.

Abstract

Current dynamical models of the slewing motion of offshore cranes cannot predict the occurring vibrations during the design phase that arise during slewing. The relatively small pedestal crane on the Sleipnir experienced severe vibrations during the slewing motion in both the crane house and the boom, which were in the order of 1 and 5 Hz. As a result, the crane operator almost shook out of his chair. This research aims to create a dynamical model of a crane from controller to suspended load to predict the occurring vibrations during slewing during the design phase. The type of crane studied is an electrically driven pedestal mounted offshore crane with a lattice boom structure.

A system analysis of the crane regarding the dynamics results in a list of dynamic effects. These are compared to obtain which dynamic effects are significant and which are negligible to include in the dynamical model. The equations of motion are derived to create the dynamical model, which consists of the controller, the slew drive system, the boom and the suspended load. The controller includes a PI-controller, a ramp function and play compensation. The ramp function creates a s-curve as speed input for the PI-controller. Play compensation brings the gears under tension to press out the play, which prevents backlash.

A comparison between a model with and without backlash shows that the model with backlash results in vibrations consisting of two frequencies, which are in the same order of magnitude as the vibrations observed in the pedestal crane on the Sleipnir. While the model without backlash is not able to predict these vibrations. In addition, the frequencies of vibration correspond to the natural frequencies of the first two lateral bending modes of the boom.

The results show that backlash in the system excites the natural frequencies of the boom. This means that the cause of the vibrations is the combination of backlash and the flexibility of the boom. The dynamical model calculates the same vibrations as were found in the pedestal crane on the Sleipnir. Thus, the proposed dynamical model can predict the occurring vibrations during slewing during the design phase. Experimental data should be obtained in the future to validate the model.

T.A. van Vugt
Delft, October 2020

Nomenclature

Parameter	Description	Unit
k_θ	Rotational stiffness	Nm/rad
c_θ	Rotational damping	Nms/rad
k_δ	Lateral stiffness	N/m
c_δ	Lateral damping	Ns/m
θ	Rotational displacement	rad
δ	Lateral displacement	m
b	Width	m
h	Height	m
L	Length	m
r	Radius	m
D	Outer diameter	m
d	Inner diameter	m
t	Thickness	m
w	Distance from centre line	m
A	Area	m^2
α	Boom angle	rad
Δ_b	Backlash	rad
I	Area moment of inertia	m^4
I_t	Torsional constant	m^4
J	Mass moment of inertia	kgm^2
M	Mass	kg
m	Mass per unit length	kg/m
F	Force	N
T	Torque	Nm
g	Gravitational constant	m/s^2
E	E-modulus	N/m^2
G	Shear modulus	N/m^2
f	Frequency	Hz
ω	Frequency	rad/s
τ	Time	s
i	Transmission ratio	
ϕ	Phase shift	
Z	Number of teeth	
ν	Poisson ratio	
N	Number of	
ζ	Damping ratio	
Subscripts		
n	Natural	
t	Tooth	
h	Crane house	
COG	Centre of gravity	
cr	Critical	
p	Pinion	
r	Ring gear	
s	Sun gear	
b	Boom	
C	Compression	
eq	Equivalent	

l	Load
m	Motor
d	Drives
gb	Gearbox
wr	Wire rope

Contents

List of Figures

List of Tables

1

Introduction

The world is in a transition from oil and gas to renewable energy and so is the offshore environment. Unused offshore platforms are being decommissioned, while wind turbines are being installed at a rapid pace. Offshore crane are required to accommodate both the decommissioning and the installation. The largest crane vessel, the Sleipnir, was built to decommission unused platforms. The cranes on this vessel set an astonishing record for heaviest lift of 15300 tonnes [1].

Huisman Equipment built and designed the cranes on the Sleipnir and these are shown in Figure 1.1. This shows two large tub mounted cranes on the left, which are used for decommissioning. A smaller crane is encircled on the right and Figure 1.2 zooms into this crane. This crane type is a pedestal mounted offshore crane and it has a lattice boom structure. Such a crane has three motions, one of which is the slewing motion, which is the rotation of the crane house around its own axis.

This master thesis is conducted at the dynamics group at Huisman Equipment. The main activity of Huisman is designing and building offshore cranes.

Figure 1.1: Largest crane vessel, the Sleipnir with two 10000 tonnes tub cranes on the left and one 100 tonnes pedestal mounted offshore crane encircled on the right

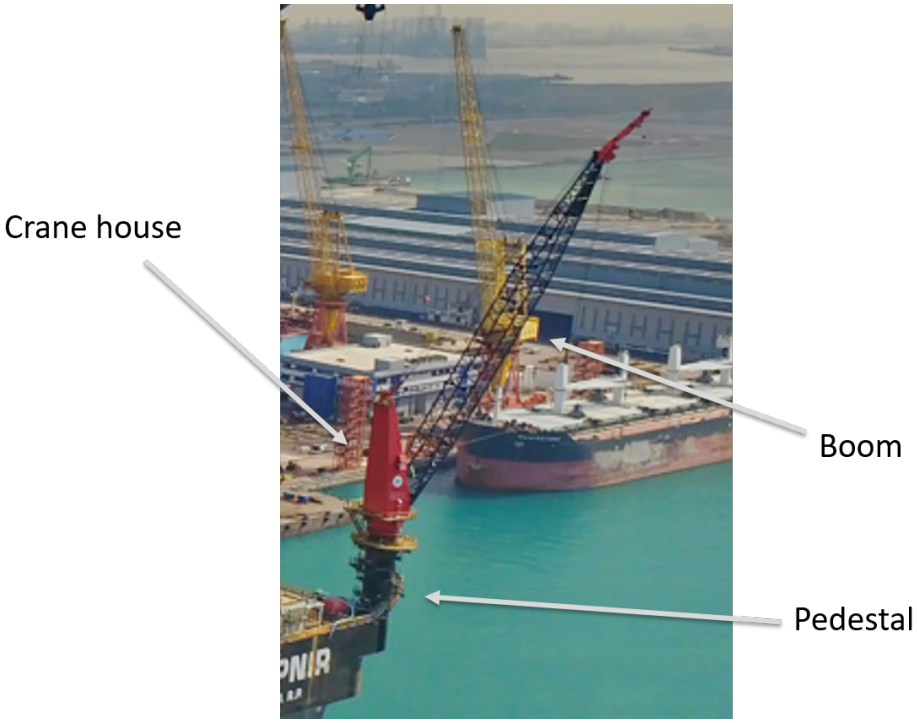

Figure 1.2: The pedestal mounted offshore crane on the Sleipnir. The crane house is built on the pedetal. Connected to the crane house is the boom

1.1. Problem statement

The pedestal crane shown in Figure 1.2 experienced heavy vibrations during the slewing motion in both the crane house and the boom. These vibrations occurred during starting and stopping of the crane and consisted of two frequencies. The first one is a low frequent vibration, in the order of $1\ Hz$. The second frequency is more high frequent and in the order of $5\ Hz$. These vibrations were a problem, because of the following three reasons:

- The operator almost shook out of his chair
- The structure will fatigue more quickly
- The load positioning accuracy cannot be guaranteed

The problem is that the current calculation models are not able to predict the vibrations that occurred during the slewing motion. The current models include the following:

- Boom as one equivalent rotating inertia
- Static sidelead of the load
- Static heel of the crane
- Static friction

These models calculate the required slewing moment to accelerate the boom while including static forces. The standards provide dynamic amplification factors to account for dynamics. Thus a dynamic analysis, which can predict vibrations during slewing, is missing. It is inefficient to solve vibration issues after building a crane, because it costs a lot of money and time. Furthermore, it can cause dangerous situations for the crane operator and the people around the crane. Therefore, it is desirable to be able to predict vibrations during the design phase.

The objective of this master thesis is to develop a method to predict the occurring vibrations during the slewing motion in a pedestal crane during the design phase. This requires a dynamical model that simulates the response of the crane during slewing to predict vibrations. The research question is defined as follows:

How to model the dynamics of a slew drive system of offshore cranes sufficiently accurate to predict the occurring vibrations during slewing during the design phase of a crane?

Other researchers investigated crane dynamics during slewing before, however, important aspects were neglected. Section 1.2 presents the literature review to show what has been done and what is missing. The main research question is divided into sub-questions to break up the problem is smaller problems, which are defined as follows:

- Which components are used during the slewing motion?
- Which dynamic effects are significant to predict vibrations during slewing?
- How can a theoretical dynamical model be created to test certain dynamic effects for significance?
- How should the theoretical model be simplified, such that the approximation is sufficiently accurate?

This thesis considers an electrically driven pedestal mounted offshore crane with a lattice boom structure. The pedestal crane on the Sleipnir is a hydraulically driven pedestal crane with a lattice boom structure. There have also been cases where an electrically driven crane experiences the same sort of vibrations as occurred in the Sleipnir. The vibrations of an electrically driven crane have typically a slightly higher frequency, because a hydraulic crane has an additional stiffness as a result of the oil. This additional stiffness term decreases the equivalent stiffness, which decreases the natural frequency. The electrically driven crane is considered, because most new cranes use an electric drive. A few assumptions are made for this thesis:

- The manufacturing and assembly is done according to the drawings and there are no failures
- The controller works well and is stable
- The effect of vessel motions due waves is not included, because this has typically a period of 6 to 15 seconds

1.2. Literature review

There are multiple researchers that analysed the crane dynamics during the slewing motion. For example Jerman et al. [12] and Blackburn et al. [2] created a dynamical model of the crane with the assumption that the boom and drive line is rigid. In addition, Jerman and Kramar [11] assumed that the boom only has axial flexibility, hence, neglecting lateral bending, while also assuming a rigid drive line. Other researchers used a flexible boom with a single stiffness, hence adding one extra natural frequency to the model, while also assuming the drive line to be rigid [4][10]. Yang et al. [25] and Rauscher and Sawodny [18] created the same models with the only difference that the payload can move over the length of the boom.

The dynamics of multiple pinions driving a ring gear is analysed for tunnel boring machines. Here, the stiffness of the gearboxes and backlash is included in the dynamical models [22][16][23][19]. However, these researches did not include the dynamics of the crane itself.

Thus, the current research regarding crane dynamics during slewing neglects the dynamics from the following:

- Slew drive system
- Controller
- A boom with higher order bending modes than the first mode

A model that considers the dynamics during the slewing motion from the controller to the load has not been researched before. This master thesis researches such a model.

1.3. Reading guide

Chapter 2 investigates the dynamic effects present in the system and analyses which dynamic effects should be included in the dynamical model. Chapter 3 explains the model, which is created to predict the dynamic slewing behaviour of the crane. Chapter 4 discusses how to model the boom sufficiently accurate and it discusses the influence of backlash and the control functions. Chapter 5 presents the conclusion of this master thesis with future recommendations.

2

System analysis

This chapter investigates the dynamic effects present in the crane during the slewing motion. Section 2.1 presents the criteria to judge whether a dynamic effect is significant or negligible. Section 2.2 shows the main components of the slew drive system and the crane. Sections 2.3 to 2.9 investigate the dynamic effects present of the main components and section 2.10 concludes which dynamic effects should be modelled and which can be neglected.

2.1. Criteria

As mentioned in section 1.1, the frequency of vibration of the Sleipnir is between 1 and 5 Hz and the electric drive is slightly more stiff than the hydraulic drive line. Therefore, the frequency range of vibration is extended to the order of magnitude of 1 to 10 Hz.

Vibrations are a result of the product of a structure and an excitation. There are two types of excitation, one with a frequency close to the natural frequency of the structure and the other excites the natural frequencies of the structure, e.g. a shock load. The criteria to judge whether a part of the crane or an excitation is significant are as follows:

- Is the natural frequency of the part of the structure in the order of magnitude of the frequency of the vibration that occurs?
- Is the frequency of excitation in the order of magnitude of the natural frequencies of the structure?
- Does the excitation excite the natural frequencies of the structure?

The first criterion corresponds to the structure and the last two correspond to the excitation. If a criterion is answered with yes, then the dynamic effect or part of the structure should be taken into account in the dynamical model. In addition, a relative error of 5% is accepted, for engineering.

2.2. Components

Figure 2.1 shows the main components used for the slewing motion. Here, the motors receive their power from the generator on the vessel. A rectifier and an inverter transform the power from the generator, such that the right frequency and voltage is sent to the motor. The motor has two outgoing shafts, one connected to the disk brake and the other drives the gearbox. The disk brake is used to keep the crane stationary. The gearbox drives the pinion, which drives the slewing ring. The crane house is assembled on top of the slew bearing. The crane house and boom are linked via a pivot. Finally, the boom transports the tackle with load during the slewing motion.

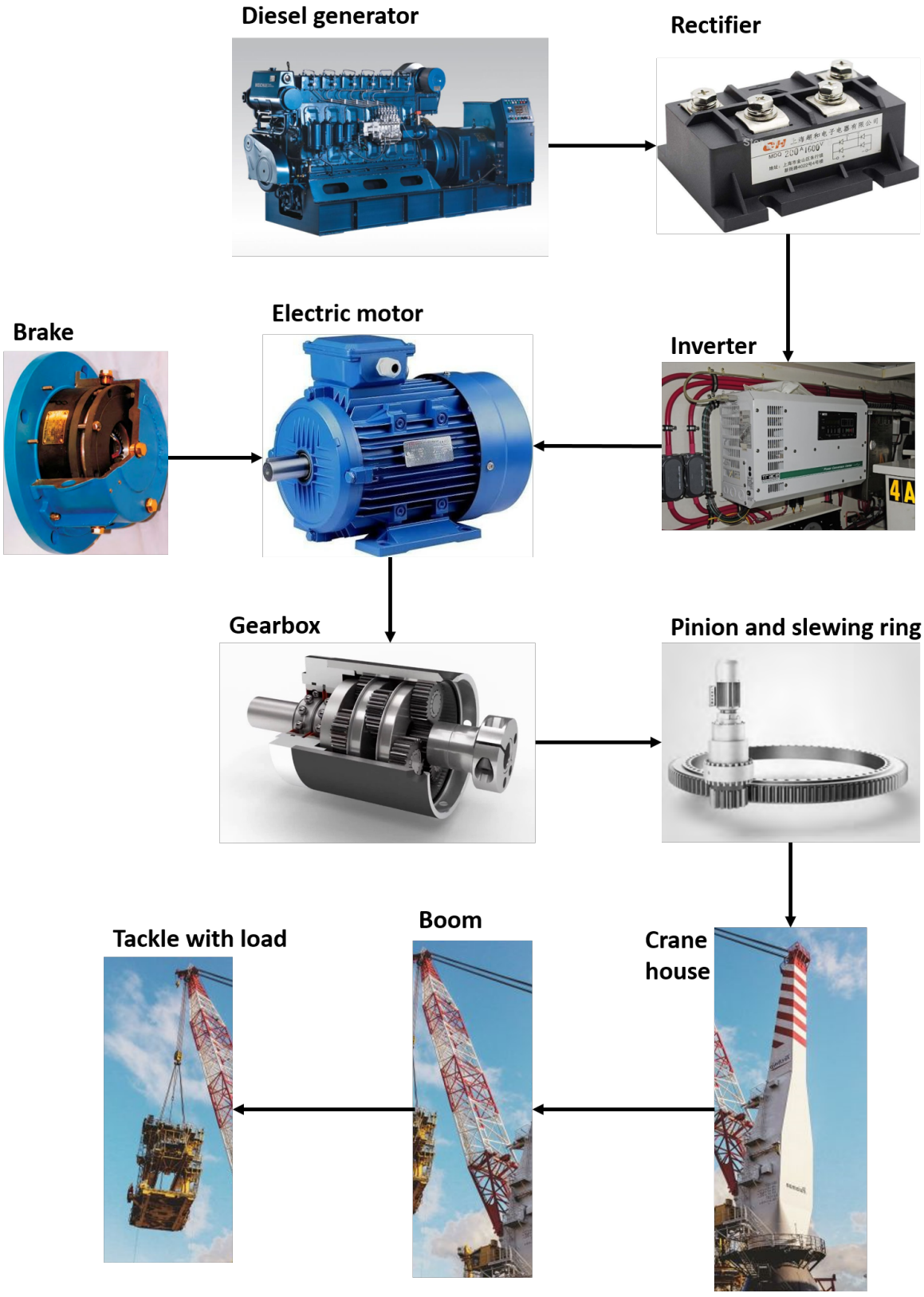

Figure 2.1: Main components used during slewing. The the rectifier and inverter transform the power from the generator for the motor. The motor drive the slew bearing via a gearbox and pinion. The crane house is built on top of the slew bearing and the boom is linked with a pivot to the crane house

Currently, the generator is typically either a diesel of LNG generator, depending which is present on the vessel. Batteries might replace the diesel and LNG generators for future vessels. A flywheel, batteries or super capacitors are used for peak power. The generator delivers a three-phase AC voltage. The rectifier transforms AC to DC with the desired voltage. The inverter uses pulse width modulation, with a switching frequency in the order of a few kHz, to transform DC back to AC with the desired frequency. Thus, the purpose of the generator, rectifier and inverter is to create the right voltage and frequency as input for the electric motor. This thesis considers a three-phase asynchronous motor, also called an induction motor, which is regulated by a variable frequency drive (VFD). Typically, the pedestal crane uses a three stage planetary gearboxes for the slewing motion. The slew drive system consists of multiple inverters, brakes, motors and gearboxes.

2.3. Controller

Figure 2.2 shows the motor control scheme that Huisman uses for the slewing motion. The control scheme divides the motors into two motor groups. Each motor has its own inverter and droop control in case of large projects, meaning motors with more than $60\ kW$, which is the case in this thesis. The crane operator requests a velocity set-point, *Speed*. The velocity first goes through a ramping function, *Ramp*, to create a s-curve of the requested velocity. An offset is generated based on the required torque, which is translated into a speed offset via the droop control. Appendix D shows an example of this droop control to compensate the play. The speed offset is subtracted from the desired velocity of one group and added to the desired velocity of the other group to compensate the play in the gears. The principle of the play compensation is that both groups deliver a counteracting torque, such that the gears are always under tension. Using this principle, the play is pressed out of the system as long as the groups have enough capacity to deliver a counteracting torque. The details of play compensation are given in Appendix B, which also shows an enlarged version of Figure 2.2.

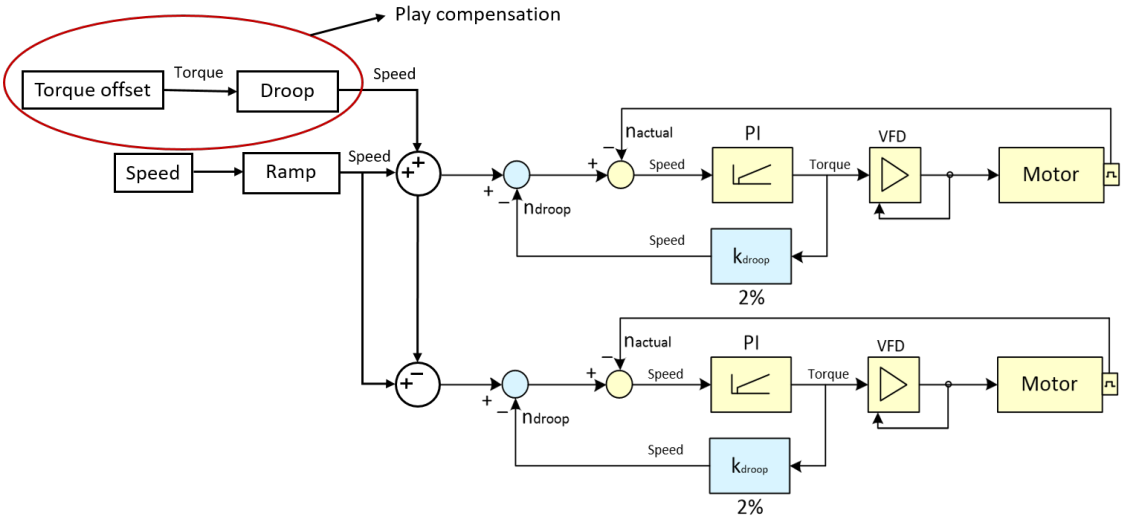

Figure 2.2: Control scheme of the slewing motors. The speed input goes through a ramp function to create a s-curve. A speed offset is generated such that the play in the system is compensated. The PI-controller calculates the required torque from the speed error. The VFD translates the required torque to input of the motor.

Thus, the speed input consists of both the ramp function and the play compensation. The ramp function creates a s-curve and the play compensation determines a speed offset to compensate the play. Afterwards, this speed input is sent to the PI-controller of the two motor groups. Encoders measure the motor speed and returns it to calculate a speed error. The PI-controller translates this error into the required torque. The VFD translates the required torque to the input for the motor. Furthermore, the k_{droop} creates a static speed offset by multiplying the normalised torque with a factor and is elaborated in Appendix D. The aim of this static offset is to minimise the difference in delivered torque in one motor group, while allowing some speed difference between the motors. In case one motor delivers more torque than the other, it is slowed down to reduce its delivered torque.

A proper VFD has a time constant around 10 milliseconds, which is much quicker than the natural

frequencies of the system. Therefore, the VFD will not influence the dynamics of the drive system significantly. The droop control creates a static speed offset depending on the torque of each motor. As long as the system has no significant deviations, which is assumed in this thesis, this offset remains static. Consequently, the droop control on the motors does no influence the dynamics. Play compensation is applied to prevent the crane going through its play. This has a large benefit, because it reduces the shock load in the system caused by backlash.

2.4. Motor with source and load sharing characteristics

An asynchronous motor contains electrical dynamics, namely, two electromechanical frequencies as a result of the inductances in the motor. This thesis assumes that the power electronics and the control work properly. This means that these electromechanical frequencies do not influence the dynamics significantly as long as this assumption holds.

The generator sends the power to the motor with with a rectifier and inverter in between. The switching frequency of the pulse width modulation in the inverter is in the order of a few kHz, which is far outside the frequency range of the occurring vibrations. A modern diesel generator and rectifier have the ability to deliver a smooth AC and DC voltage, respectively. Therefore, the generator, rectifier and inverter do not influence the dynamics of the system, as long as the power electronics work properly. With an eye on the future, the diesel generator might be replaced with batteries, which also have the ability to deliver a smooth voltage as long as the power electronics and the controller work properly.

Multiple motors are used for the slewing motion and controlled in such a way that the slewing load is shared and the effects of gear play is minimised. The load sharing characteristics are analysed of multiple pinions driving a cutter head by Wei et al. [22]. The analysis for the slew drive system is essentially the same, because the slew drive system is also a large ring gear driven by multiple motors. Between the ring and the motors are gearboxes with a spring like behaviour. The analysis is performed by solving the equations of motion obtained from Figure 2.3. The authors state that each drive can deliver a slightly different torque, causing an uneven load distribution, the following two causes are discussed:

- It is impossible to create exactly the same drives, meaning, there will be some small deviation in the inertia of the motor and the stiffness of the gearbox, among other things
- The gearbox has a time varying mesh stiffness, which is elaborated in section 2.6

The deviation between separate motors and gearboxes is assumed to be negligible during the design phase. The play compensation creates a torque offset between the two motor groups on purpose. Therefore, the load sharing between the two groups influences the dynamics significantly as a result of the play compensation.

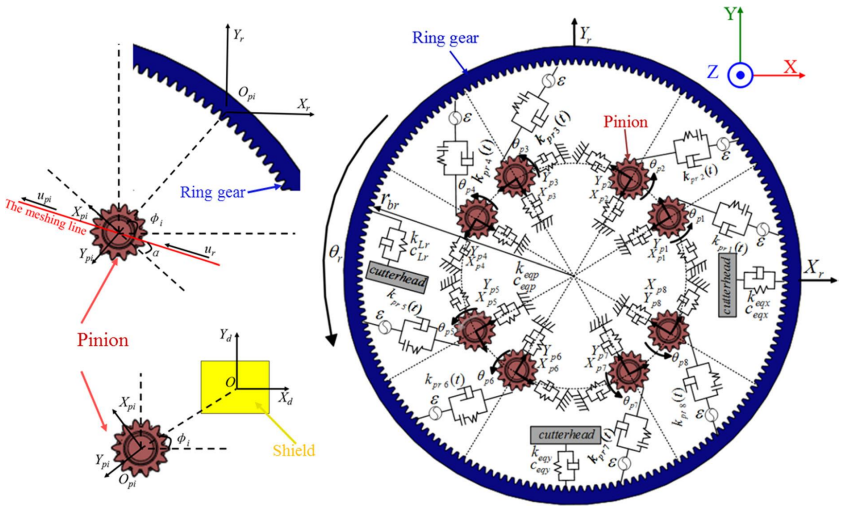

Figure 2.3: Illustration multiple pinions driving cutter head ring [9]

Thus, the electrical dynamics can be neglected in this thesis. The motors are rotating masses, which share the load according to the control functions.

2.5. Brake

Normally, a disk brake is used in cranes, which consists of rotating and stationary plates, as shown in Figure 2.4. During braking, these plates are pressed together such that a large frictional force acts on the system.

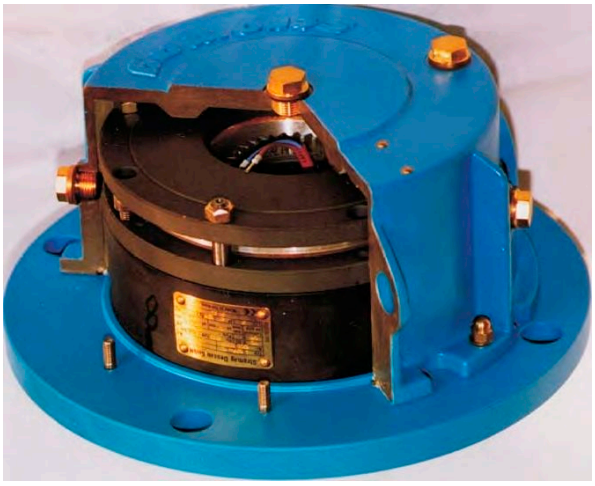

Figure 2.4: Disk brake obtained from Stromag

The electric motors are used as brakes during normal operation. The disk brakes are used to statically hold the load, the moment that the crane is stationary. These brakes are used as dynamic brakes only in case of a complete electrical power failure. The crane needs to come to a halt as quickly as possible during this emergency. Therefore, the brake will deliver a large torque. This can result in a large impact on the structure, which can excite its natural frequencies.

In addition, it is possible that the plates of the brake are not evenly pressed against the stationary plates. Consequently, the load distribution is asymmetric. In this case, shear forces are induced in the shaft on which the brake is assembled. These shear forces can cause the shaft to bend. Vibrations can occur in the shaft as a results of the time variety of the shear force.

The specifics of the dynamic effects of the brake is outside the scope of this thesis. Thus, this thesis assumes that the brake can be simplified as a rotating mass, which can deliver a torque on the motors.

2.6. Gearbox and pinion with slewing ring

Helsen et al. [7] created different models of a multistage planetary gearbox used for wind turbines with increasing complexity. The authors state that the following dynamic effects from the gearbox can influence the system:

- Inertia of the gearbox
- Gear mesh stiffness
- Backlash

The gear mesh stiffness is the equivalent stiffness as a result of the finite stiffness of the gear teeth. Backlash occurs as a results of play between the gear teeth, which is visualised in Figure 2.5. There is play in both the gearbox and between the pinion and the slewing ring gear. Therefore, backlash can occur and lead to shock loading in the system. A structure will vibrate at its natural frequencies as a result of this shock load.

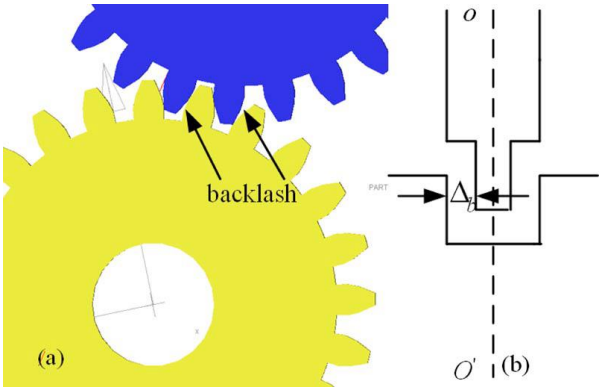

Figure 2.5: Illustration backlash with Δ_b [16]

Besides backlash, the gearboxes and pinions experience more nonlinear dynamics, which are analysed by Wang et al. [21]. They created a simplified gear model, as shown in Figure 2.6. They conclude that the gear mesh stiffness, as described above, also has a time varying contribution. Figure 2.7 shows the time variety of the mesh stiffness, mainly as a result of different number of teeth in contact. The time varying mesh stiffness is approximated using the first harmonic Fourier series [9]. The number of teeth in contact varies between two and three teeth. Thus the average stiffness is two and a half times the single tooth stiffness and varies approximately between two and three times the single tooth stiffness. Therefore the amplitude of the first harmonic is approximated as 20% of the average stiffness. The time varying stiffness can be approximated by: [9]

$$k_{\theta,mesh}(\tau) \approx \overline{k_{mesh}}(1 + 0.2sin(2\pi f_{mesh}\tau + \phi_{mesh})) \tag{2.1}$$

Here, $\overline{k_{mesh}}$ is the average mesh stiffness. The friction between the teeth results in a decreasing efficiency of the gearbox. The author state that the friction between tooth faces contribute insignificantly to the dynamics compared to the gear mesh stiffness and backlash. Therefore, this is negligible for a dynamical model.

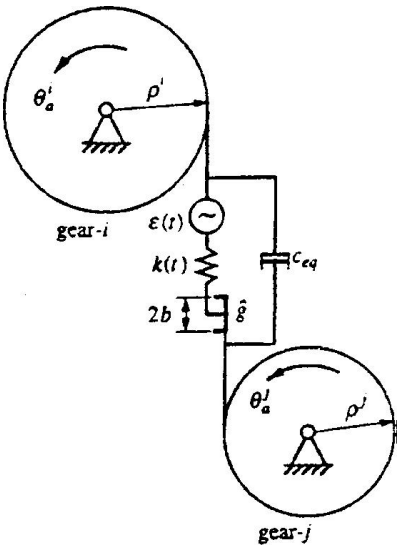

Figure 2.6: Illustration of a simplified dynamic model of gears [21]

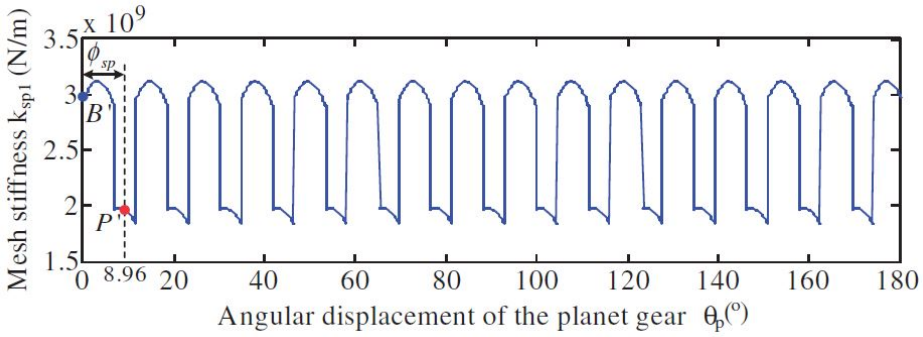

Figure 2.7: Mesh stiffness as a function of the gear angle [17]

The mesh frequency in a planetary gearbox is determined from kinematic relationships as a function of the rotational velocity of the sun gear, f_s: [17]

$$f_{mesh} = \frac{Z_r Z_s}{Z_r + Z_s} f_s \tag{2.2}$$

and the mesh frequency of the pinion is determined by: [17]

$$f_{mesh} = Z_p f_p \tag{2.3}$$

Table 2.1 gives the numerical data of typically used gearboxes and pinions and an average frequency. The mesh frequency of the pinion is $1.2\ Hz$ and the mesh frequency of the gearbox is $150\ Hz$.

Z_r	110
Z_s	8
f_s	20 Hz
Z_p	12
f_p	0.1 Hz

Table 2.1: Numerical data to determine the mesh frequency of the gearbox and pinion

Thus, the dynamic effects present in both the gearbox and the pinion are as follows:

- Inertia of the gearbox
- Backlash
- Time varying mesh stiffness

2.6.1. Comparison of play contribution from the gearbox and pinion

The play of the gearbox and the play of the pinion are compared to find whether one or the other is negligible. Appendix A provides an approximation of the play in the gearbox. Here, a range of gearboxes are shown with a transmission ratio in the range of 60 and 550. The play of these gearboxes on the outgoing axis is between 0.09°and 0.15°. The play of the pinion is approximated using the manufacturing tolerances, which are a play between 2% and 4% of the module of the pinion. This number is divided by the radius of the pinion to obtain the play in terms of rotational play. Typically, the module is 24 millimetres and the radius of the pinion is 180 millimetres. Thus, the pinion play is typically between 0.15° and 0.31°. The play in the gearbox and the pinion play is in the same order of magnitude. Therefore, both contributions should be considered.

2.6.2. Comparison of stiffness of the gearbox and pinion

The stiffness of the gearbox and the pinion are compared as two springs in series. Therefore, the component with the smallest stiffness is the dominant term. Appendix A shows that the stiffness of the gearbox is in the range of 10 to $40\ MNm/rad$ on the outgoing axis. Liang et al. [17] provided a method

to approximate the mesh stiffness of the pinion analytically. The following two contributions are the most significant to the stiffness of the pinion: [17]

- Hertzian contact stiffness
- Bending stiffness

According to the Hertzian law, the elastic compression of two isotropic elastic bodies can be approximated by two parabolic bodies in the vicinity of the contact point [17]. Figure 2.8 visualises the contribution of the Hertzian contact stiffness to the deformation of a gear on the left and the contribution of bending of the tooth is shown on the right with its cross section.

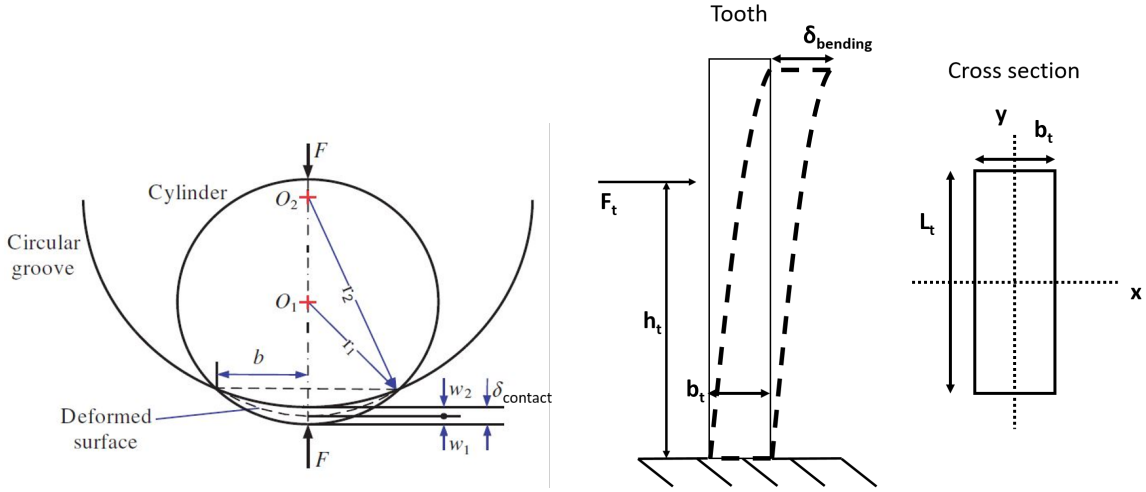

Figure 2.8: Two contributions to pinion stiffness. On the left deformation, $\delta_{contact}$, as a result of Hertzian contact stiffness and on the right deformation, $\delta_{bending}$, as a result of bending stiffness

The deformation of a tooth as a result of the Hertzian contact stiffness is determined by: [17]

$$\delta_{contact} = \frac{4F_t(1-\nu^2)}{\pi E b_t} \tag{2.4}$$

and the deformation as a result of the bending stiffness is calculated by: [24]

$$\delta_{bending} = \frac{F_t h_t^3}{3EI_{yy}} \approx \frac{F_t h_t^3}{3E\frac{1}{12}L_t b_t^3} = \frac{4F_t h_t^3}{EL_t b_t^3} \tag{2.5}$$

These two contributions to the total deformation are in series [17]. The rotational deformation of the pinion as a result of the deformation of the teeth is determined using geometry. The rotation of the gear equals to the deformation of the teeth divided by the radius of the gear. Thus, the rotational deformation of the pinion is determined by:

$$\theta_p = \frac{\delta_{contact} + \delta_{bending}}{r_p} \tag{2.6}$$

As mentioned before, on average 2.5 teeth are in contact. Therefore, the average torque delivered by the pinion, T, equals to 2.5 times the force on one tooth times the radius of the pinion. Thus, the stiffness of the pinion can be approximated by:

$$k_{\theta,p} = \frac{T}{\theta_p} = \frac{2.5Fr_p}{\frac{\delta_{contact}+\delta_{bending}}{r_p}} = 2.5r_p^2 \frac{\pi E L_t b_t^3}{4(1-\nu^2)L_t b_t^2 + 4\pi h_t^3} \tag{2.7}$$

Table 2.2 shows the numerical data to determine the stiffness of a commonly used pinion. The stiffness is calculated to be $713\ MNm/rad$, which is much larger than the stiffness of the gearbox (between 10 and $40\ MNm/rad$). Therefore, the pinion can be assumed to be infinitely stiff compared to the gearbox.

ν	0.3
L_t	200 mm
r_p	180 mm
h_t	50 mm
b_t	70 mm

Table 2.2: Numerical data to determine the stiffness of the pinion

2.7. Crane house

The crane house is loaded in torsion via the rotation of the boom and in bending due to the wire rope at the top of the crane house. During slewing, the force in the wire rope is static, while the rotation of the crane house is dynamic. Therefore, only the rotational dynamics of the crane house are considered.

The crane house is simplified as a thin walled hollow cylinder. Figure 2.9 shows a schematic representation of the crane including the dimensions. Here, D_h is the average diameter of the crane house and h_{pivot} is the height from slewing axis to pivot connecting of the boom.

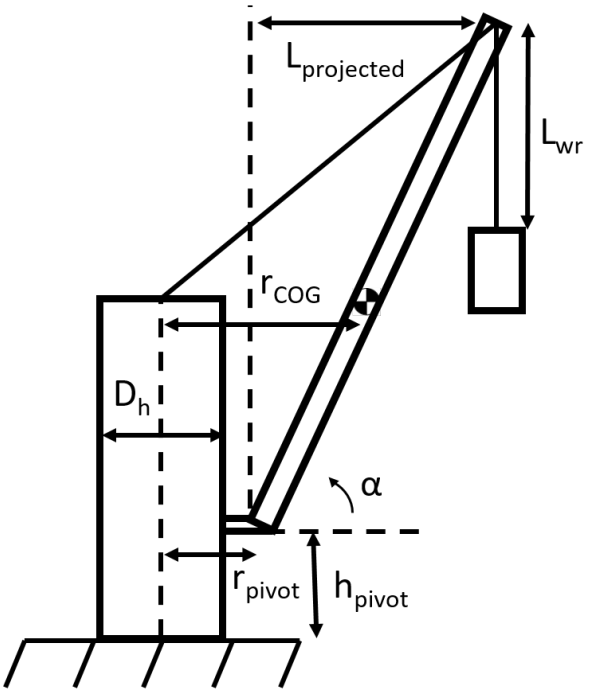

Figure 2.9: Schematic representation of the side view of the crane including the dimensions used during the calculations

The rotational inertia of the crane house is approximated using the thin walled hollow cylinder approximation and can be calculated as follows: [24]

$$J_h \approx \frac{1}{4} M_h D_h^2 \tag{2.8}$$

The rotational stiffness of the crane house is calculated by: [24]

$$k_{\theta,h} = \frac{GI_h}{h_{pivot}} \approx \frac{\pi}{8} \frac{GD_h^3 t_h}{h_{pivot}} \tag{2.9}$$

Table 2.3 shows the numerical data of the crane house of the crane used during this thesis. Here, the inertia of the crane house is $2.52 \cdot 10^5\ kgm^2$ and the rotational stiffness is $34.9\ GNm/rad$. The natural frequency of the crane house is approximated by: [24]

$$f_{n,h} = \frac{1}{2\pi} \sqrt{\frac{k_{\theta,h}}{J_h}} \tag{2.10}$$

and is determined to be approximately $59\ Hz$.

Parameter	Value
M_h	138000 kg
D_h	2.7 m
G	81 GPa
t_h	0.12 m
h_{pivot}	2.15 m

Table 2.3: Numerical data of the crane house

2.8. Boom

Figure 2.10 represents the lattice boom structure schematically and on scale. This shows the three main loading terms, which are the following:

- The slewing moment, M_{slew}, as a result of the slewing motion
- A lateral force, F_{load}, as a result of the swinging motion of the load
- A compressive load, F_C, as a result of the mass of the load and the boom angle

The distance from the centre line of the boom to the cords is significantly larger than the average distance over the length of the boom from the bracings to the centre line. In addition, both the outer diameter and the thickness of the cords are typically more than 1.5 and 3 times as large with respect to the bracings, respectively. Therefore, the contribution of the parallel axis theorem is much larger of the cords than the bracings. As a result, the cross section is simplified by considering the cords only, as shown in Figure 2.11. The following equation approximates the area moment of inertia using the cross section: [24]

$$I_{yy,b} = \frac{\pi}{16}(D_b^4 - d_b^4) + \pi w_b^2 (D_b^2 - d_b^2) \tag{2.11}$$

Figure 2.10 shows that the distance from the centre line of the boom to the middle of the cords vary over its length. The total width (equals to $2w_b$) of the most left part of the boom is 4500 millimetres, while the most right part has a total width of 1830 millimetres. Consequently, the area moment of inertia $I_{yy,b}$ varies significantly over the length of the boom, which influences the bending rigidity of the boom over its length.

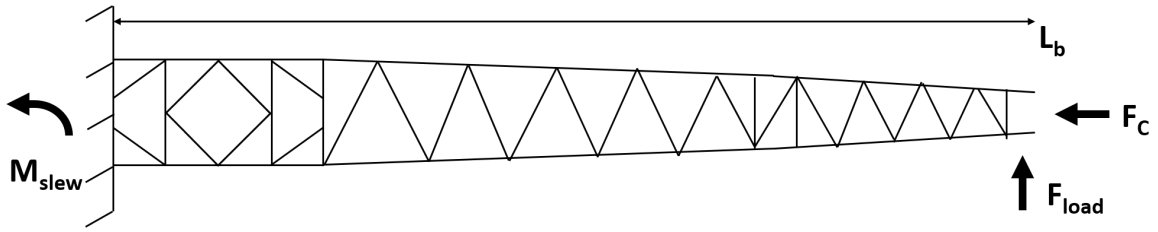

Figure 2.10: Schematic representation of a boom with lattice structure including the loading terms, the slewing moment M_{slew}, the force from the swinging of the load, F_{load} and the compressive load from the weight of the load, F_C

The boom shown in Figure 2.10 has a length of 46.6 metres and a ratio length over width between 10 and 25 depending on the location on over its length. Therefore, the length is significantly larger than the width, hence, beam theory is applicable. In addition, the deformation of the boom remains small, meaning small angle approximation holds. Thus, linear beam theory is applicable.

The natural frequencies of the boom can be approximated by simplifying the boom as a homogeneous beam while using the average width, $\widetilde{w_b}$. The equivalent lateral bending stiffness of a homogeneous beam can calculated using: [24]

$$k_{\delta,b} = \frac{3EI_{yy,b}}{L_b^3} \tag{2.12}$$

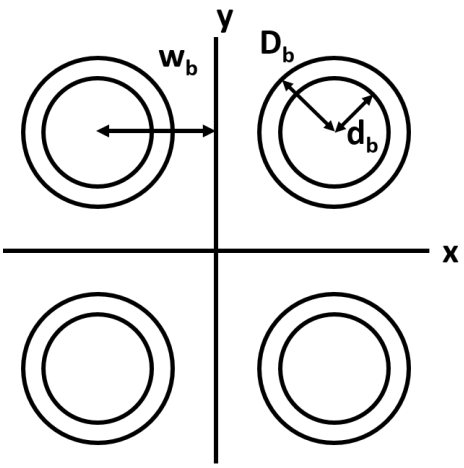

Figure 2.11: Simplified cross section of the boom

and the equivalent rotational inertia of the boom around the slewing axis is approximated by: [24]

$$J_b = \frac{1}{12} M_b((2w_b)^2 + L_{projected}^2) + M_b r_{COG}^2 \tag{2.13}$$

The natural frequencies of the boom can be determined by the following equation: [15]

$$f_{n,b} = \frac{y_t^2}{2\pi} \sqrt{\frac{EI_{yy,b}}{M_b L_b^3}} \tag{2.14}$$

In this equation, the first three values for y_t are considered to calculate the first three natural frequencies. The first three values are: [15]

$$y_t = \begin{bmatrix} 1.875 \\ 4.694 \\ 7.855 \end{bmatrix}$$

Table 2.4 shows the numerical values of the crane with a boom angle of $\alpha°$ and Table 2.5 shows the first three natural frequencies corresponding to the first three bending modes of a beam, which are visualised in Figure 2.12

Parameters	Value	Parameters	Value
$\widetilde{w_b}$	1.47 m	M_b	81047 kg
D_b	267 mm	r_p	3.6 m
d_b	227 mm	α	50°
E	210 GPa	$L_{projected}$	$L_b cos(\alpha)$
L_b	46.6 m	r_{COG}	$r_{pivot} + \frac{1}{2} L_{projected}$

Table 2.4: Numerical values of the case study

Bending mode	Natural frequency [Hz]
1	1.0
2	6.5
3	18.3

Table 2.5: First three natural frequencies of the boom modelled as clamped beam

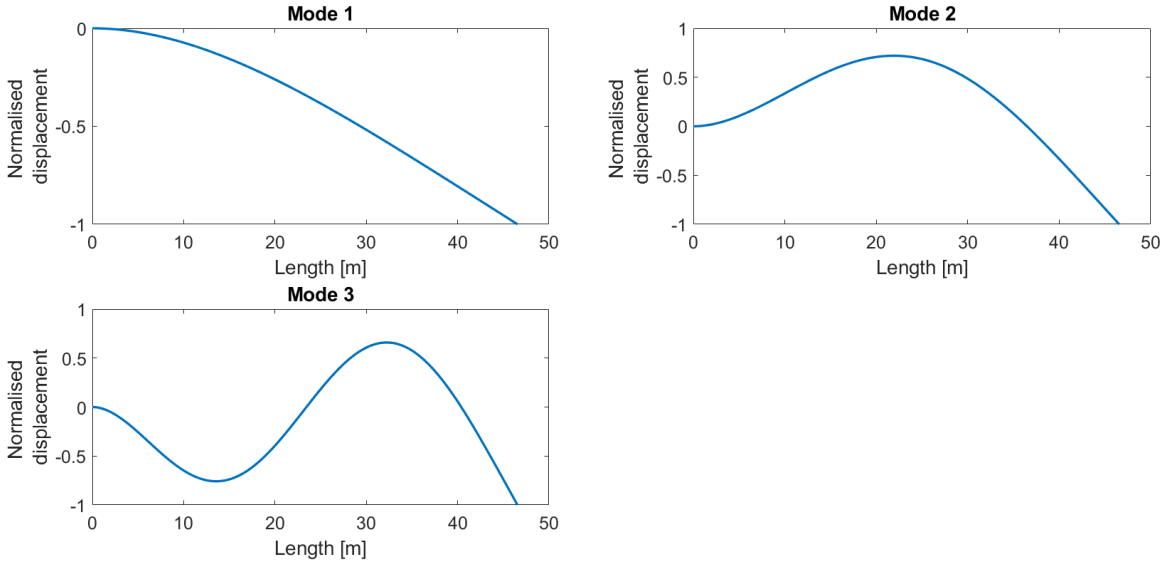

Figure 2.12: First three bending modes of a beam corresponding to the first three natural frequencies. Here, top left is the first natural frequencies, top right, the second and left below the third one

Valle et al. [20] analysed the consequences of a beam under compression on its natural frequencies. They concluded that the natural frequencies of a beam can decrease when it is subject to compressive loading, F_C, and can be calculated with the following equation:

$$f_{n,C}(F_C) = f_{n,b}\sqrt{1 - \frac{F_C}{F_{cr}}} \tag{2.15}$$

Here, F_{cr} is the critical buckling load and f_n is the natural frequency without compression, as calculated by Equation 2.14.

Now, the change in natural frequency is calculated when the compressive load is considered to find out whether this has a significant influence. The critical buckling load, F_{cr}, is calculated as follows: [24]

$$F_{cr} = \frac{\pi^2 E I_{yy,b}}{L_b^2} \tag{2.16}$$

This equation holds when linear beam theory is applicable, which is the case for the boom. The critical buckling load is calculated to be $287\ MN$, when using the numerical values given by Table 2.4. The maximum allowable axial force for this boom is $8.5\ MN$, which means that the maximum value of $\sqrt{1 - \frac{F_C}{F_{cr}}}$ is 0.97. Thus, the natural frequencies of the boom decrease with less than 3% as a result of the compressive load, which is insignificantly small.

2.9. Tackle with load

Figure 2.13 shows a schematic top view of the crane with a load at the tip of the boom. Here, the two directions of motion of the load are shown, namely offlead and sidelead. The dashed line represents the path of the load during slewing. This shows that the main motion of the load during slewing is in the sidelead direction. Therefore, offlead can be neglected.

The load can be simplified as a single or double pendulum, as shown in the left and right of Figure 2.14, respectively. A model with the double pendulum motion has the added value that the positioning of the lower block or e.g. a monopile can be modelled. This is relevant, because the pedestal crane on the Sleipnir showed that the lower block could not be positioned accurately as a result of the vibrations in the crane.

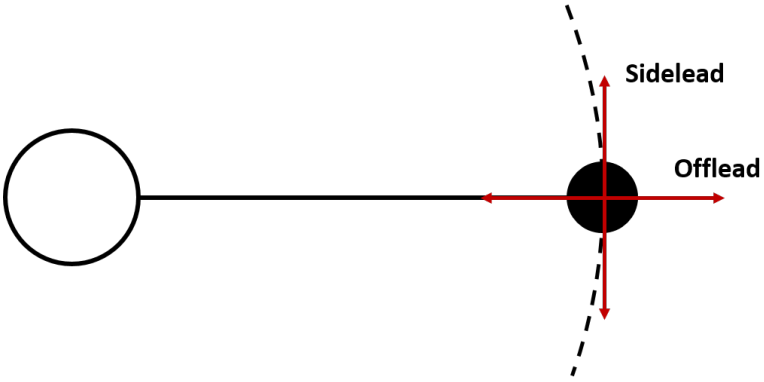

Figure 2.13: Top view of the crane with the load as a solid dot on the right, the boom as a straight line in the middle and the slewing ring as a circle on the left. The dashed line represent the slewing path

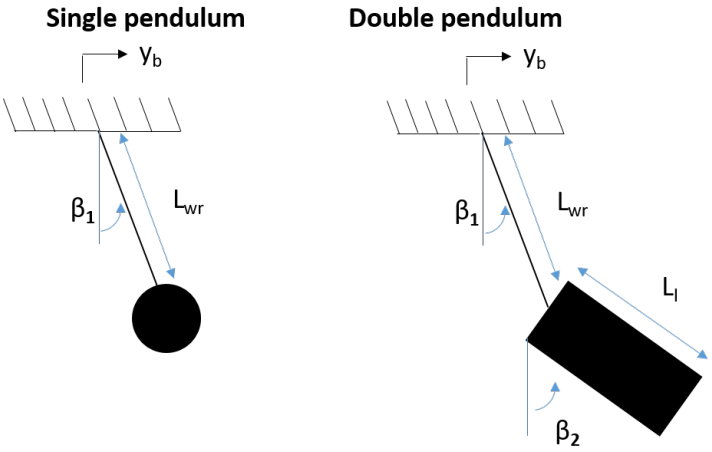

Figure 2.14: Schematic representation of the load as a single pendulum (left) and as a double pendulum (right)

The following equation approximates the natural frequency of a single pendulum: [24]

$$f_{n,l} = \frac{1}{2\pi}\sqrt{\frac{g}{L_{wr}}} \tag{2.17}$$

The suspended length of the load, L_{wr}, is variable and typically more than 5 metres. Therefore, the natural frequency of the swinging motion remains lower than $0.2\ Hz$. The load also consists of the double pendulum motion. The length of e.g. a lower block can be much less than the suspended length. A rough approximation of the natural frequency of the lower block itself is by simplifying it as a single pendulum, hence neglecting the wire rope to which it is connected. Typically, the length of the load is less than 1 metres, which means a natural frequency of $0.5\ Hz$, when calculated with (2.17). The distributed mass and the connection with the wire rope results the natural frequency to be a bit higher [6]. Therefore, it can be expected that the natural frequency of the double pendulum remains less than $1\ Hz$.

2.10. Comparison dynamic effects and conclusion

Section 2.7 showed that the rotational inertia of the crane house equals to $2.52{\cdot}10^5\ kgm^2$. The rotational inertia of the boom is lowest at its maximum boom angle of $80°$and equals to $5.23 \cdot 10^6\ kgm^2$. Even at the highest boom angle, the relative deviation between the inertia of the crane house and boom is 4.8%. Thus, the inertia of the crane house is negligibly small compared to the inertia of the boom.

The inertia of the brake, electric motor and gearbox are shown in Table 2.6. Here, the relative deviation is defined as the deviation between the inertia of the whole drive line and only the inertia of

the motor. This relative deviation is 7.5%, which means that the inertia of all three components should be considered.

Component	Inertia [kgm^2]
Motor	1.08
Brake	0.037
Gearbox	0.05

Table 2.6: Inertia of separate components in the drive line

The inertia of the drive line on the fast axis of the motor is $1.17\ kgm^2$. The transmission ratio of the gearbox is 215.4 and the pinion is 12.7. The inertia of the drive line on the rotating axis of the boom equals to $1.17(215.4 \cdot 12.7)^2 = 8.76 \cdot 10^6\ kgm^2$. The rotational inertia of the boom is between $5.23 \cdot 10^6$ and $7.32 \cdot 10^7\ kgm^2$, depending on the boom angle. The inertia of the drive line and the boom are in the same order of magnitude. Thus, both should be considered.

The stiffness of the gearbox results in a natural frequency between the drive line and the boom. The drive line and boom are two rotating masses with the gearbox as stiffness in between, as visualised in Figure 2.15. This figure simplifies the boom as a rigid body. On the right of this figure, the system is simplified such that the natural frequency can be determined with: [24]

$$f_{n,gb} = \frac{1}{2\pi}\sqrt{\frac{k_{\theta,gb}}{J_{eq}}} \tag{2.18}$$

In this equation, the equivalent inertia, J_{eq}, is calculated as follows:

$$J_{eq} = \frac{1}{\frac{1}{J_{driveline}} + \frac{1}{J_b}} \tag{2.19}$$

The gearbox considered in this thesis has a stiffness of $6900\ kNm/rad$ on the outgoing axis of the gearbox. This means that the stiffness of the gearbox equals to $6900 \cdot 12.7^2 = 1.11 \cdot 10^6\ kNm/rad$ after the transmission ratio of the pinion. The boom angle is $50°$ in this case to use an average boom angle. This leads to an equivalent inertia, J_{eq}, of $6.96 \cdot 10^6\ kgm^2$ and a natural frequency of $2.0\ Hz$ as a result of the gearbox stiffness.

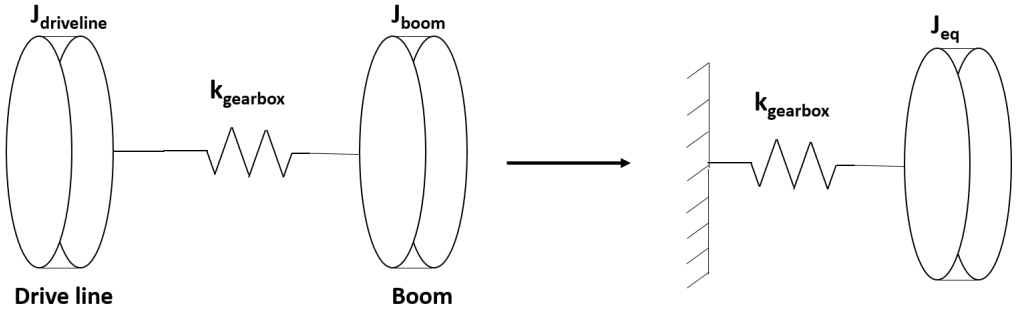

Figure 2.15: Schematic representation of the crane as two rotating masses (left) representing the drive line and the boom respectively. On the right the equivalent system to determine the natural frequency as a result of the gearbox stiffness

The occurring vibrations are in a frequency range of 1 and $10\ Hz$, as stated in section 2.1. Table 2.7 shows the frequencies present in the system, and the following can be concluded:

- The mesh frequency of the gearbox is outside the range of the occurring frequencies
- The natural frequency of the crane house is outside the range of the occurring frequencies
- The natural frequency as a result of the gearbox stiffness and the natural frequency of the boom are in the range of the occurring frequencies

- The natural frequency of the swinging of the load is too small to cause vibrations
- The natural frequency of the double pendulum can be excited as a result of the occurring vibrations

The pedestal crane on the Sleipnir also showed that the lower block was vibrating as a result of the vibrations in the boom.

Dynamic effect of component	Frequency [Hz]
Mesh frequency gearbox	150
Natural frequency crane house	59
First three natural frequencies boom	1.0; 6.5; 18.3
Natural frequency caused by gearbox stiffness	2.0
Natural frequency of the swinging motion of the load	< 0.2
Natural frequency double pendulum	< 1.0

Table 2.7: Summary of frequencies in the system

Table 2.8 summarises the dynamic effects present and which ones should be included in the model to predict vibrations in a crane.

Component	**Dynamic effect**	**Consider in model?**
Controller	PI-control	Yes
	Play compensation	Yes
	Ramp function	Yes
	k_{droop}	No
	VFD	No
Motor with source and load sharing characteristics	Inertia	Yes
	Electrical dynamics including the source	No
	Load sharing characteristics between two motor groups	Yes
Brake	Inertia	Yes
	Time varying braking torque	No
Gearbox and pinion	Inertia	Yes
	Gear mesh stiffness of the gearbox	Yes
	Gear mesh stiffness of the pinion	No
	mesh frequency	No
	Backlash	Yes
Crane house	Inertia	No
	Stiffness	No
Boom	Inertia	Yes
	Variable bending stiffness	Yes
	First few lateral bending modes	Yes
	Torsion	Yes
	Decreasing bending frequencies from the compressive load	No
Tackle with load	Sidelead	Yes
	Offlead	No
	Double pendulum behaviour	Yes

Table 2.8: Summary of dynamic effects including which to neglect and which to consider

3

Dynamical model and verification

This chapter discusses the software possibilities and the usage of the frequency and time domain in section 3.1 and 3.2, respectively. Section 3.3 derives the equations of motion of the slew drive system, boom and load separately and section 3.4 presents the verification of the mechanical model. Section 3.5 describes the motor control scheme. Finally, section 3.6 derives the final equations of motion to give a mathematical description of the whole crane.

3.1. Software

There are two main types of programming environment that can be used, namely, multi body software packages, e.g. Motion View and numerical computing environments like MATLAB. Table 3.1 presents a few pros and cons of multi body software and numerical computation tools. Multi body software consists of black boxes, which result in less feeling with the underlying dynamics and modelling choices. This is a disadvantage, because it is desired to be able to model specific dynamic effects and to test the significance of this specific effect.

	Pros	Cons
Multi body software	Easy modelling possible Quick modelling Lower probability to make mistakes	Model consists of black boxes Computation time
Numerical computation	Ability to model specific dynamics Computation time	In depth understanding required

Table 3.1: Pros and cons of multi body software and numerical computation software

This research aims to find out which dynamic effects should be modelled to predict the occurring vibrations during slewing. Here, it is desired to be able to model specific dynamic effects and to test the influence of individual effects. In addition, it is desired to be able to perform multiple tests in a relatively short time. Therefore, numerical computation environmental is most suitable. This research uses MATLAB, because this is both a powerful program and it is available.

3.2. Frequency domain and time domain

The models can be solved in both the frequency and time domain. The main advantages of the frequency domain analysis are as follows:

- Computationally efficient
- Quick method to assess system response spectrum
- Provides natural frequencies and eigenmodes directly

The main advantages of the time domain analysis are the following:

- Nonlinear terms can be included
- The transient response can be computed

The frequency domain is strong in quickly calculating the natural frequencies and the eigenmodes in a system and is used for this purpose. However, it cannot include nonlinear effects, while the crane consists of nonlinear dynamics, like backlash. Therefore, time domain simulations are also required.

3.3. Model of the mechanical system

Numerical computations require a set of equations of motion of the crane. The crane has quite a lot of degrees of freedom, which leads to a large set of equations. Therefore, the mechanical system is broken done into three subsystems, which are the:

- Slew drive system
- Boom
- Suspended load

An additional advantage of breaking up the system is that these subsystems can be verified separately using analytical comparisons. After creating these separate models, the interaction between the models is derived using the finite element matrix assembly method. Chapter 2 presented the dynamic effects that should be included in these separate models. Figure 3.1 and Figure 3.2 show schematically the top and view of the crane, respectively. Here, on the left, the crane house with six motors are shown, in the middle the lattice boom structure and at the right the load.

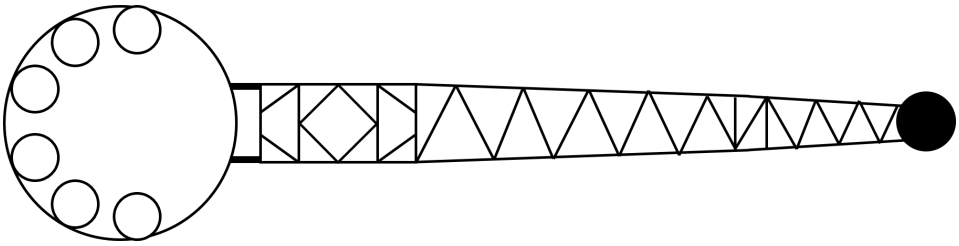

Figure 3.1: Schematic top view op the crane

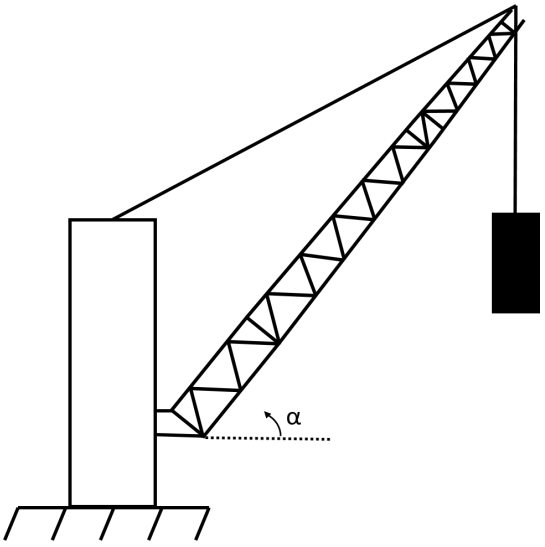

Figure 3.2: Schematic side view op the crane

3.3.1. Slew drive system

The slew drive system for the slewing motion consists of the following dynamics, which follow from chapter 2:

- Inertia of the motors, gearboxes and brakes
- Load sharing characteristics
- Stiffness of the gearbox
- Backlash of the gearbox and pinion

Figure 3.3 represents the slew drive system schematically. Here, two motors are shown, in reality, there are N_m motors, which typically is 6. The spring, $k_{gb,i}$, and damper, $c_{gb,i}$, represent the gearbox and the spring includes backlash, Δ_b.

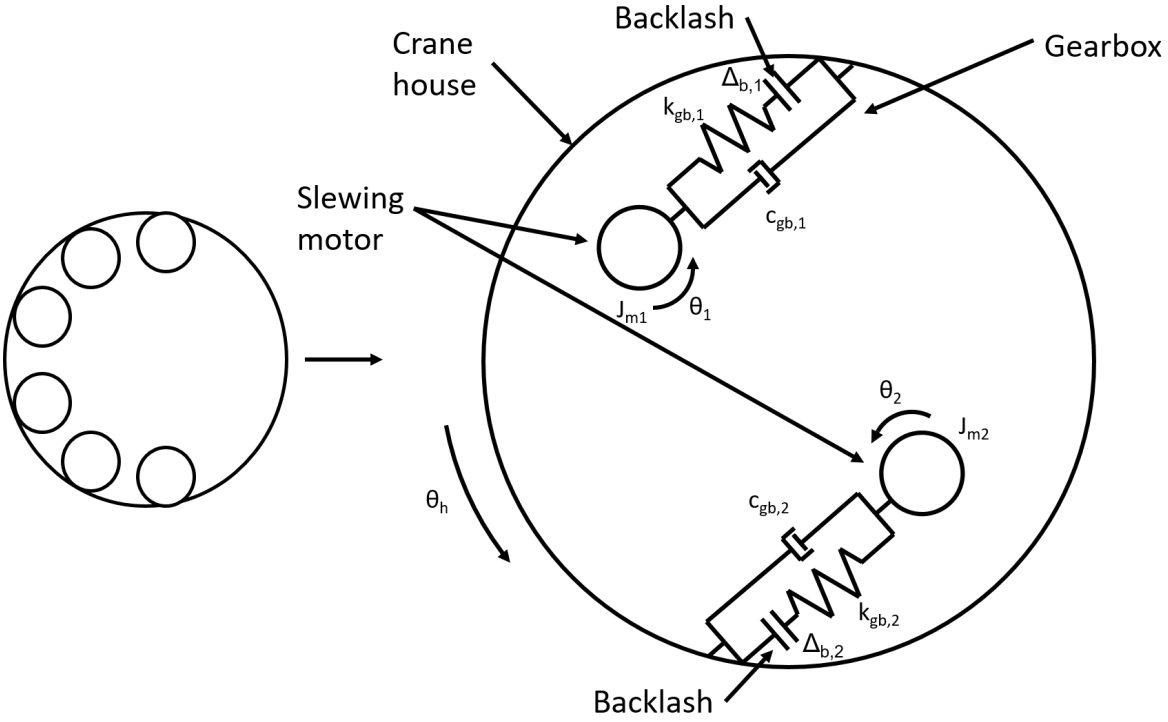

Figure 3.3: Schematic representation of the slew drive system

The equations of motion of the three rotating bodies shown in Figure 3.3 are derived using the displacement method. The equation of motion of motor group i is given by:

$$J_{m,i}\ddot{\theta}_{m,i} = k_{\theta,gb,i}(\theta_h - \theta_{m,i}) + c_{\theta,gb,i}(\dot{\theta}_h - \dot{\theta}_{m,i}) \tag{3.1}$$

Here, i is the number of the motor group. The equation of motion of the crane house is:

$$J_h\ddot{\theta}_h = \sum_{i=1}^{N_m} k_{gb,i}(\theta_{m,i} - \theta_h) + \sum_{i=1}^{N_m} c_{gb,h}(\dot{\theta}_{m,i} - \dot{\theta}_h) \tag{3.2}$$

These two equations can be translated into the mass and stiffness matrix for a variable number of motors. The mass matrix is given by:

$$[M_d] = \begin{bmatrix} J_{m,1} & 0 & \dots & 0 & 0 \\ 0 & J_{m,2} & \dots & 0 & 0 \\ 0 & 0 & \ddots & 0 & 0 \\ 0 & 0 & \dots & J_{m,N_m} & 0 \\ 0 & 0 & \dots & 0 & J_h \end{bmatrix} \tag{3.3}$$

and the stiffness matrix is given by:

$$[K_d] = \begin{bmatrix} k_{gb,1} & 0 & \dots & 0 & -k_{gb,1} \\ 0 & k_{gb,2} & \dots & 0 & -k_{gb,2} \\ 0 & 0 & \ddots & 0 & \vdots \\ 0 & 0 & \dots & k_{gb,N_{gb}} & -k_{gb,N_{gb}} \\ -k_{gb,1} & -k_{gb,2} & \dots & -k_{gb,N_{gb}} & \sum_{i=1}^{N_{gb}} k_{gb,i} \end{bmatrix} \tag{3.4}$$

The damping matrix has exactly the same shape as the stiffness matrix. The damping in the gearbox is highly complex and can be simplified by assuming a damping ratio of 3% [9].

Backlash changes the shape of the torque transmitted through the gearbox as a function of its deformation, as visualised in Figure 3.4. Here, the region where the gearbox is within its play, the gears are not in contact. This means that there is no torque transmitted and the stiffness is zero. The torque transmitted by the gearbox with backlash is given by: [16]

$$T_{gb,i}(\Delta\theta) = \begin{cases} k_{gb,i}(\Delta\theta_i - \Delta_b), & \text{if } \Delta\theta_i > \Delta_b \\ k_{gb,i}(\Delta\theta_i + \Delta_b), & \text{if } \Delta\theta_i < -\Delta_b \\ 0, & \text{else} \end{cases} = k_{gb,i}\Delta\theta_i \begin{cases} (1 - \frac{\Delta_b}{\Delta\theta_i}), & \text{if } \Delta\theta_i > \Delta_b \\ (1 + \frac{\Delta_b}{\Delta\theta_i}), & \text{if } \Delta\theta_i < -\Delta_b \\ 0, & \text{else} \end{cases} \tag{3.5}$$

In this equation T_i is the torque transmitted through the spring with the subscript i which denotes the i^{th} gearbox, $\Delta\theta_i$ denotes the difference between the rotational displacement of the crane house and the i^{th} motor. To use this equation with the equations of motion, it needs to be rewritten as follows:

$$T_{gb,i}(\Delta\theta) = \widetilde{k}_{gb,i}\Delta\theta_i \tag{3.6}$$

Here, $\widetilde{k_{gb,i}}$ is the stiffness of the gearbox with backlash included, as visualised in Figure 3.5 and is given by:

$$\widetilde{k_{gb,i}} = k_{gb,i} \begin{cases} (1 - \frac{\Delta_b}{\Delta\theta_i}), & \text{if } \Delta\theta_i > \Delta_b \\ (1 + \frac{\Delta_b}{\Delta\theta_i}), & \text{if } \Delta\theta_i < -\Delta_b \\ 0, & \text{else} \end{cases} \tag{3.7}$$

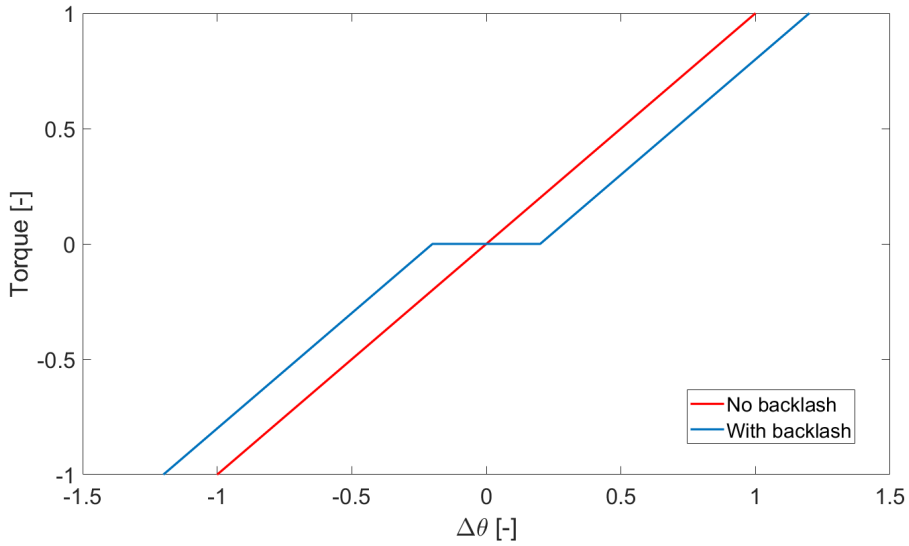

Figure 3.4: Torque in a spring as a function of the rotational difference between two gears with backlash in blue and without backlash in red

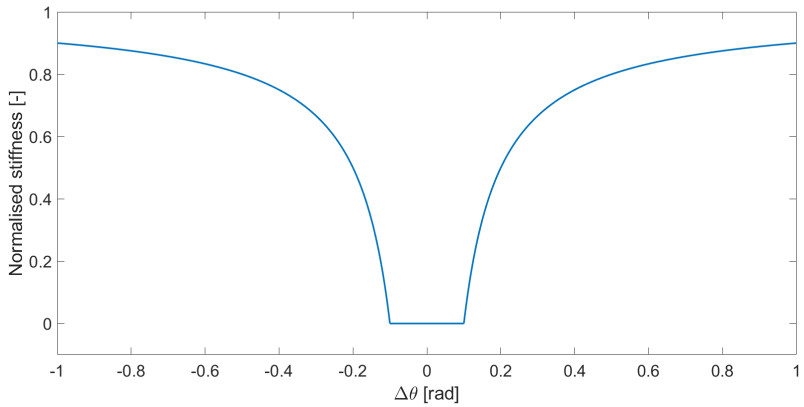

Figure 3.5: Transformed stiffness to include backlash in the springs. The stiffness is normalised and as a function of the normalised rotational difference between two gears including backlash

3.3.2. Boom

The boom including fly jib during the slewing motion consists of the following dynamics, as given in chapter 2:

- Inertia
- Variable bending stiffness over its length
- First few lateral bending modes
- Torsion with eccentric force cause by the fly jib

As mentioned in section 2.8, linear beam theory holds for the boom. In addition, it showed that the third natural frequency of the boom is $18.3\ Hz$, which means that higher order modes will have a natural frequency outside the range of occurring frequencies. As a result, only the first few natural frequencies are required in the model of the boom. It is assumed that the cross section of the boom remains perpendicular to the neutral axis. Therefore, the Euler-Bernoulli beam theory is sufficient for the model of the boom [14].

The boom is modelled using multiple Euler-Bernoulli beam elements to model the first few bending modes. Figure 3.6 shows the schematic side and top view of the boom. The axis system shown in this figure corresponds to the rotating frame of the crane house. In this figure, the black dots represent the nodes, which are connected to create the beam elements. The number of nodes is parametric in the model, such that N_{nodes} are modelled. The pivot connection of the boom with the crane house is stiff, therefore, a clamped boundary condition at the most left node is used.

The mass and stiffness matrices corresponding to each element are derived using the method of weighted residuals. The mass matrix of one beam element subject to lateral bending is given by: [8]

$$[M_{bending}] = \frac{m_b L_b}{420}\begin{bmatrix} 156 & 22L_b & 54 & -13L_b \\ 22L_b & 4L_b^2 & 13L_b & -3L_b^2 \\ 54 & 13L_b & 156 & -22L_b \\ -13L_b & -3L_b^2 & -22L_b & 4L_b^2 \end{bmatrix} \tag{3.8}$$

and the stiffness matrix for one element subject to lateral bending is given by: [8]

$$[K_{bending}] = \frac{EI_b}{L_b^3}\begin{bmatrix} 12 & 6L_b & -12 & 6L_b \\ 6L_b & 4L_b^2 & -6L_b & 2L_b^2 \\ -12 & -6L_b & 12 & -6L_b \\ 6L_b & 2L_b^2 & -6L_b & 4L_b^2 \end{bmatrix} \tag{3.9}$$

The states in these matrices are $[y_{left},\ \phi_{left},\ y_{right},\ \phi_{right}]^T$. Here, the elements are represented by the left and right node of one element.

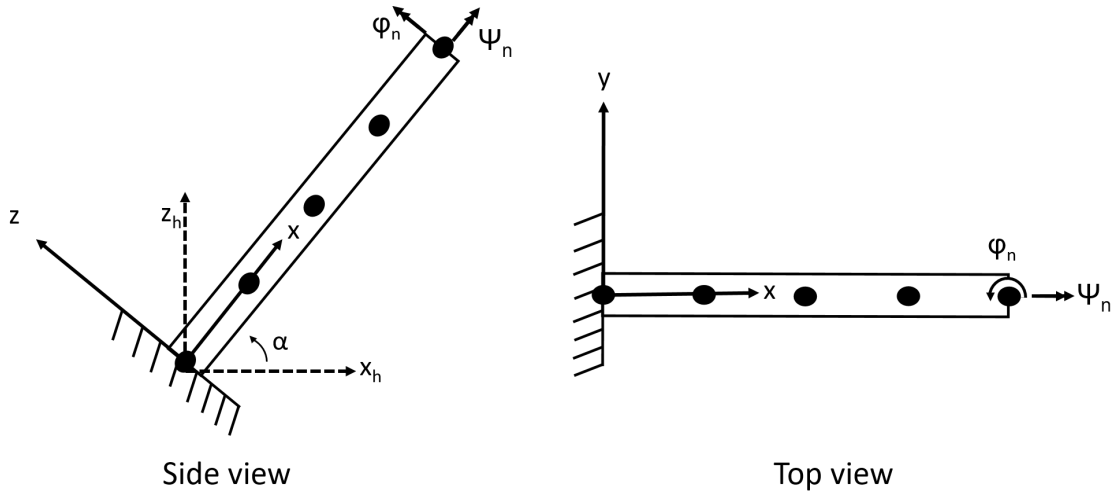

Figure 3.6: Schematic representation of the boom from the side view on the left with the boom angle and on the right the top view. The black dots denote the nodes (5 are shown) and each node has three degrees of freedom, y, ϕ and ψ. The axis of the boom are given with x, y, z and rotates with the slewing motion and the axis of the crane house corresponds to the dashed axis with z_h and x_h

The mass matrix of a beam element subject to torsion is calculated with: [8]

$$[M_{torsion}] = \frac{m_b L_b I_{t,b}}{6A_b}\begin{bmatrix} 2 & 1 \\ 1 & 2 \end{bmatrix} \tag{3.10}$$

and the stiffness matrix by: [8]

$$[K_{torsion}] = \frac{GI_{t,b}}{L_b}\begin{bmatrix} 1 & -1 \\ -1 & 1 \end{bmatrix} \tag{3.11}$$

Here, also the left and right states are used and denotes by $[\psi_{left},\, \psi_{right}]^T$.

The matrices for bending and torsion are combined into one matrix by rewriting the states and matrices. The final mass matrix of one beam element subject to lateral bending and torsion is given by:

$$[M_b] = \frac{m_b L_b}{420}\begin{bmatrix} 156 & 22L_b & 0 & 54 & -13L_b & 0 \\ 22L_b & 4L_b^2 & 0 & 13L_b & -3L_b^2 & 0 \\ 0 & 0 & 0 & 0 & 0 & 0 \\ 54 & 13L_b & 0 & 156 & -22L_b & 0 \\ -13L_b & -3L_b^2 & 0 & -22L_b & 4L_b^2 & 0 \\ 0 & 0 & 0 & 0 & 0 & 0 \end{bmatrix} + \frac{m_b L_b I_{t,b}}{6A_b}\begin{bmatrix} 0 & 0 & 0 & 0 & 0 & 0 \\ 0 & 0 & 0 & 0 & 0 & 0 \\ 0 & 0 & 2 & 0 & 0 & 1 \\ 0 & 0 & 0 & 0 & 0 & 0 \\ 0 & 0 & 0 & 0 & 0 & 0 \\ 0 & 0 & 1 & 0 & 0 & 2 \end{bmatrix} \tag{3.12}$$

and the final stiffness matrix is given by:

$$[K_b] = \frac{EI_b}{L_b^3}\begin{bmatrix} 12 & 6L_b & 0 & -12 & 6L_b & 0 \\ 6L_b & 4L_b^2 & 0 & -6L_b & 2L_b^2 & 0 \\ 0 & 0 & 0 & 0 & 0 & 0 \\ -12 & -6L_b & 0 & 12 & -6L_b & 0 \\ 6L_b & 2L_b^2 & 0 & -6L_b & 4L_b^2 & 0 \\ 0 & 0 & 0 & 0 & 0 & 0 \end{bmatrix} + \frac{GI_{t,b}}{L_b}\begin{bmatrix} 0 & 0 & 0 & 0 & 0 & 0 \\ 0 & 0 & 0 & 0 & 0 & 0 \\ 0 & 0 & 1 & 0 & 0 & -1 \\ 0 & 0 & 0 & 0 & 0 & 0 \\ 0 & 0 & 0 & 0 & 0 & 0 \\ 0 & 0 & -1 & 0 & 0 & 1 \end{bmatrix} \tag{3.13}$$

The states corresponding to these matrices are $[y_{left},\, \phi_{left},\, \psi_{left},\, y_{right},\, \phi_{right},\, \psi_{right}]^T$.

Damping in the boom is mainly structural damping, because it is a large steel structure, hence Rayleigh damping is applicable [3]. This states that the damping can be determined from the mass and stiffness matrices:

$$[C_b] = a_0[M_b] + a_1[K_b] \tag{3.14}$$

A boom is a large steel structure, which means that the damping mainly consists of structural damping. Therefore, a_0 can be neglected and a_1 is calculated as follows: [3]

$$a_1 = \frac{2\zeta(\omega_{n,2} - \omega_{n,1})}{\omega_{n,2}^2 + \omega_{n,1}^2} \tag{3.15}$$

As mentioned in section 2.8, the bending stiffness varies over the length of the boom. Therefore, each element has its own bending stiffness corresponding to the average stiffness in the specific section of the crane corresponding to the element. The elements are connected together with the finite element matrix assembly method. Figure 3.7 shows how these elements are connected into one large matrix. This figure shows a model with 5 elements and each square represent one element matrix.

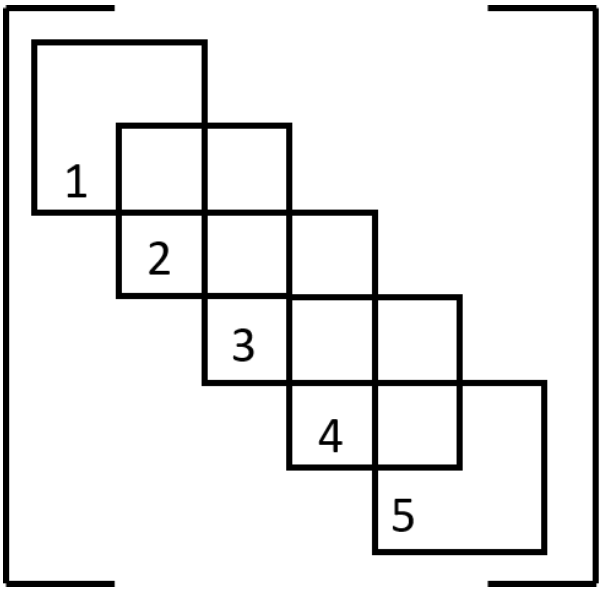

Figure 3.7: Each square represent the matrix of one element. The separate element matrices are assembled into one large matrix

The boom angle causes a rotation of the boom, as visualised in Figure 3.6. The first node of the boom, i.e. the most left node, can be rewritten in terms of the rotation of the crane house, because these nodes coincide. The kinematic relation of the degrees of freedom of these two nodes is related as follows:

$$\vec{u} = \begin{bmatrix} y_1 \\ \phi_1 \\ \psi_1 \end{bmatrix} = \theta_h \begin{bmatrix} r \\ cos(\alpha) \\ sin(\alpha) \end{bmatrix} \tag{3.16}$$

As a result of this relation, the first three rows and columns of mass, damping and stiffness matrix of the boom can be merged by including the vector $\vec{u}$. The stiffness matrix is transformed as follows:

$$[K_b] = \begin{bmatrix} \vec{u}'[K_{11}]\vec{u} & \vec{u}'[K_{12}] \\ [K_{21}]\vec{u} & [K_{22}] \end{bmatrix} \tag{3.17}$$

Here, $[K_{11}]$, $[K_{12}]$ and $[K_{21}]$ correspond to the first three rows and columns and $[K_{22}]$ corresponds to the remainder of the stiffness matrix of the boom. The mass and damping matrix are transformed using the same equation as for the stiffness matrix.

3.3.3. Load

According to chapter 2, the following should dynamics should be included in the dynamical model of the load:

- Sidelead motion
- Double pendulum motion

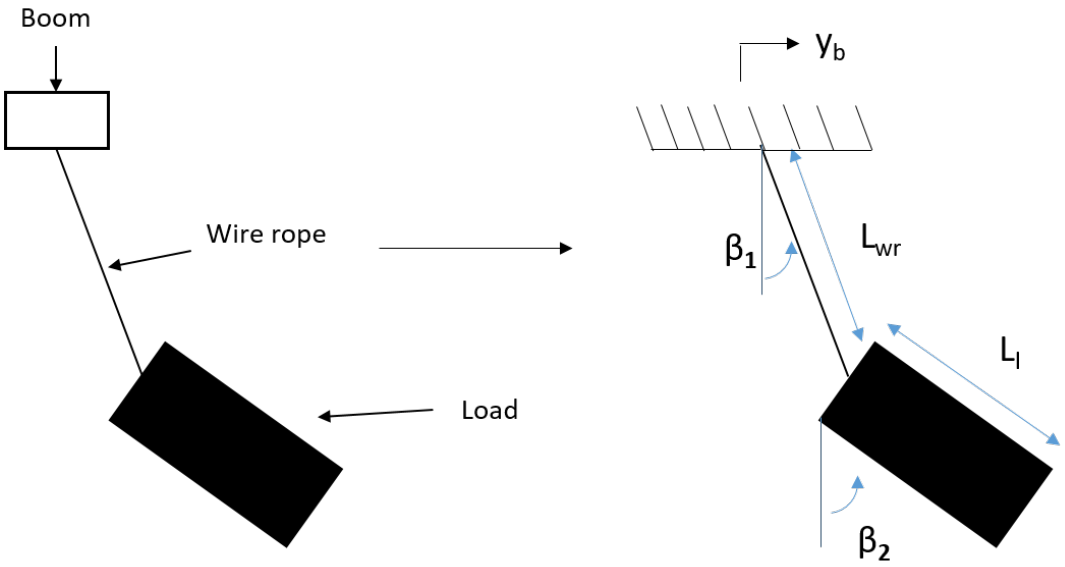

Figure 3.8: Schematic representation of the load

A schematic representation is given in Figure 3.8 with the two angles denoted as β_1 and β_2. The top of the double pendulum can move as a result of the motion of the boom.

The equations of motion are obtained via the Lagrangian method and written in matrix form [5]. The mass matrix is given by:

$$[M_l] = \begin{bmatrix} M_l & M_l L_{wr} & \frac{1}{2} M_l L_{wr} \\ M_l L_{wr} & M_l L_{wr}^2 & \frac{1}{2} M_l L_{wr} L_l \\ \frac{1}{2} M_l L_l & \frac{1}{2} M_l L_{wr} L_l & \frac{7}{12} M_l L_l^2 \end{bmatrix} \tag{3.18}$$

and the stiffness matrix of the load is given by:

$$[K_l] = \begin{bmatrix} 0 & 0 & 0 \\ 0 & M_l g L_{wr} & 0 \\ 0 & 0 & \frac{1}{2} M_l g L_l \end{bmatrix} \tag{3.19}$$

The states corresponding to the mass and stiffness matrix are $[y_b,\ \beta_1,\ \beta_2]^T$. The damping in sidelead direction equals to 0.5% of the critical damping [13].

3.4. Verification

3.4.1. Slew drive system

We verify the slew drive system using the following four verifications:

- A comparison between the natural frequency with an analytical formulation
- A comparison between the amplitude of the motors and crane house when subject to an initial displacement
- A comparison between the motion with an analytically derived equation of the motion
- With backlash, the difference in displacement should be around the value of the play

Figure 3.9 shows the steps to simplify the model of the slew drive system to be able to derive the natural frequency analytically. Here, the left shows the model of the slew drive system. The middle step merges the motors and gearboxes into one equivalent inertia en stiffness using the parallel masses and springs conversion, respectively. The last step is on the right, which shows one equivalent mass as a

result of merging the equivalent mass of the motors and the mass of the crane house. This conversion is calculated as masses in series and can be determined with:

$$J_{eq} = \frac{1}{\frac{1}{J_{eq,m}} + \frac{1}{J_h}} \tag{3.20}$$

The following equation determines analytically the natural frequency of the most right simplification: [24]

$$\omega_n = \sqrt{\frac{N_{gb} k_{gb}}{J_{eq}}} \tag{3.21}$$

Table 3.2 shows the numerical values on the fast axis of the motor. Note, this table shows that the crane house has some inertia. However, this is negligible, according to chapter 2. This inertia in included such that the mass matrix does not become singular. The analytical natural frequency equals to $5.1\ Hz$.

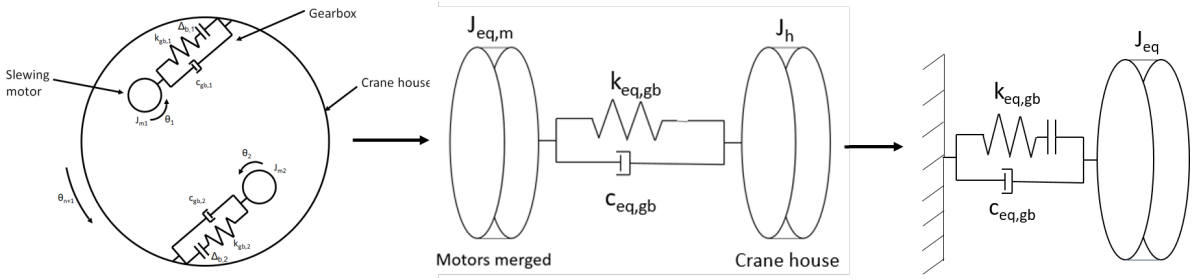

Figure 3.9: On the left, the mechanical model of the slew drive system is shown, in the middle, the motors and gearboxes are merged into one equivalent inertia and gearbox respectively with the inertia of the crane house connected to the gearbox stiffness. On the right, the two rotating masses are merged into one equivalent inertia

J_m	1.17 kgm^2
k_{gb}	149 Nm/rad
J_h	1 kgm^2
N_m	6

Table 3.2: Parameters used for the drive system

Figure 3.10 shows the response of the motor and the crane house when subject to an initial displacement of the slew bearing of $0.2\ rad$. This figure shows that the natural frequency of the system equals to $5.1\ Hz$, which is the same as analytically determined.

Figure 3.10 also shows a difference in amplitude between the slew bearing and the motors. This is a result of the difference of inertia of the different components. The ratio of the displacement of the motors and the crane house depends on the ratio of the inertia of both components and this ratio can be determined as follows:

$$\frac{\ddot{\theta}_h}{\ddot{\theta}_m} = \frac{\frac{\Delta\theta k N_m}{J_h}}{\frac{\Delta\theta k_{gb}}{J_{motor}}} = \frac{N_m J_m}{J_h} \tag{3.22}$$

The ratio equals to 7.0 and the ratio in amplitude in Figure 3.10 is 7.1, which is approximately equal to the analytically derived version.

The next step is to compare an analytically derived function of the motion with the numerically determined motion when the slew drive system is subject to a forced vibration. The numerical simulation considers all six motors as shown in the model in the left of Figure 3.9 and the analytical formulation corresponds the the middle of this figure. The torque applied on each motor is the following:

$$T(\tau) = \frac{1}{3} sin\left(\frac{\pi}{5}\tau\right), \text{ for } \tau < 10 \text{ s} \tag{3.23}$$

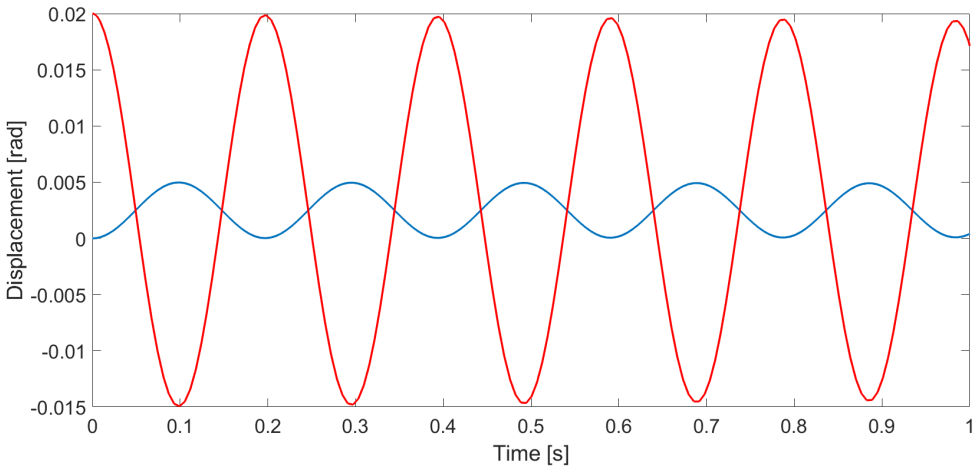

Figure 3.10: Response of the motors (blue) and slew bearing (red) when the slew bearing is subject to an initial displacement of 0.2 rad

The analytical function is found by solving the differential equation that describes the equations of motion of the motors, which is given by:

$$N_m J_m \ddot{\theta}_m + N_m k_{gb}(\theta_m - \theta_h) = T(\tau) \tag{3.24}$$

The differential equation of the crane house is given by the following equation:

$$J_h \ddot{\theta}_h + N_m k_{gb}(\theta_h - \theta_m) = 0 \tag{3.25}$$

In these two equation, the damping is neglected, because this term is small compared to the spring force. These two differential equations are solved in MATLAB using the function 'dsolve'. Table 3.2 shows the parameters of the equations, only. k_{gb} is decreased to $1\ Nm/rad$ because the deformation of the spring is too small otherwise. The analytical equation of the displacement of the motors is:

$$\theta_m = 0.397\tau - 0.597sin\left(\frac{\pi}{5}\tau\right) \tag{3.26}$$

and the displacement of the crane house is:

$$\theta_h = 0.397\tau - 0.637sin\left(\frac{\pi}{5}\tau\right) \tag{3.27}$$

The difference in amplitude results in a difference in displacement between the motors and the crane house. This is expected, because the spring needs to be under tension to transmit torque from the motors to the crane house.

Figure 3.11 shows the displacement of the motors and the crane house both numerically and analytically. This figure shows that the analytical solution coincides with the numerical solution.

The results until here excluded backlash in the slew drive system. Figure 3.12 shows the difference in displacement between the crane house and one of the motors when backlash is included and the same torque as (3.23) is applied. Figure 3.13 shows the corresponding torque transmitted through one gearbox. These two figures show the following:

- The displacement oscillates around the gear play
- The torque is zero when the gears are not in contact
- The torque suddenly increases when the gears go through their play causing a shock load

These three points are expected, because there should be no torque transmitted when the gears are not in contact. In addition, there is an impact when the gears mesh, which causes a shock load.

The four verifications show that the numerical model behaves as expected. Therefore, the model of the slew drive system simulates the dynamics included correctly.

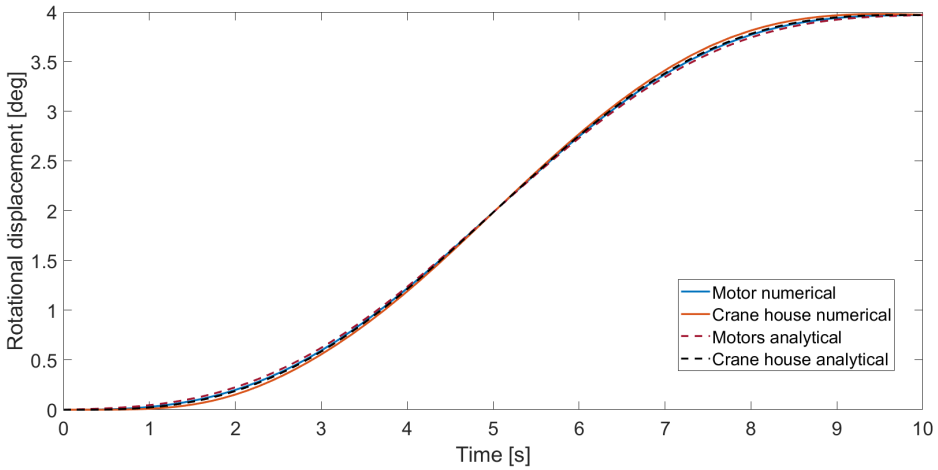

Figure 3.11: Displacement of the numerical calculation of the motor (blue) and the crane house (red) when subject to a prescribed torque. The dashed black line shows the displacement calculated analytically

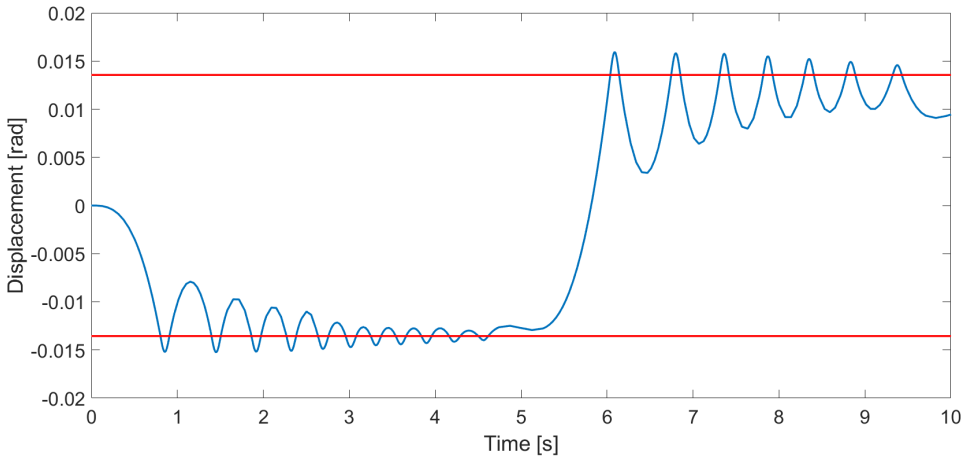

Figure 3.12: Difference in displacement between slew bearing and motor in blue and in red the play

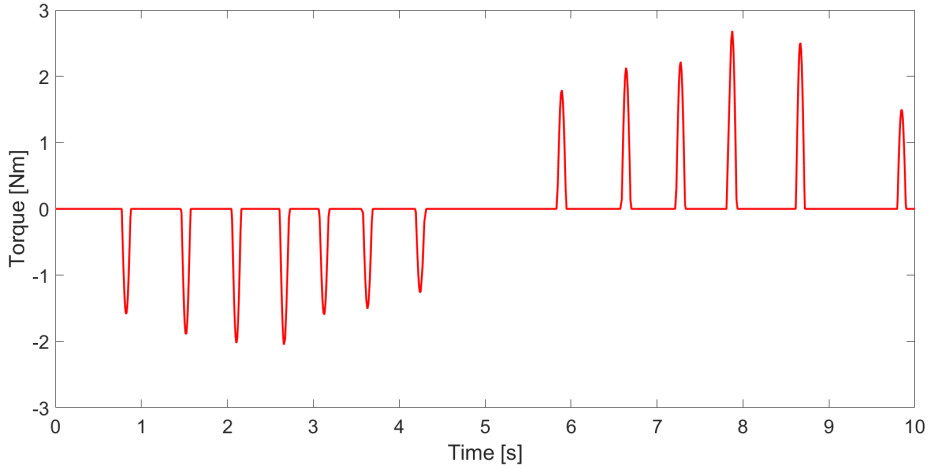

Figure 3.13: Torque transmitted by one gearbox when the system has backlash and a torque is applied on the motors and is given by (3.23)

3.4.2. Boom

Section 2.8 provides the first three natural frequencies of the boom analytically, which are compared by calculating the natural frequency of the numerical boom model in frequency and time domain.

Figure 3.14 shows the response of the displacement of the tip of the boom when it is subject to an initial displacement of 50 millimetres. An initial displacement excites the first few natural frequencies of the boom. This figure shows many frequencies the first second. Most damp out quickly and two dominant vibrations remain in the boom, which are given in Table 3.3. This table also shows the analytically derived natural frequencies from section 2.8 and the natural frequencies determined in the frequency domain.

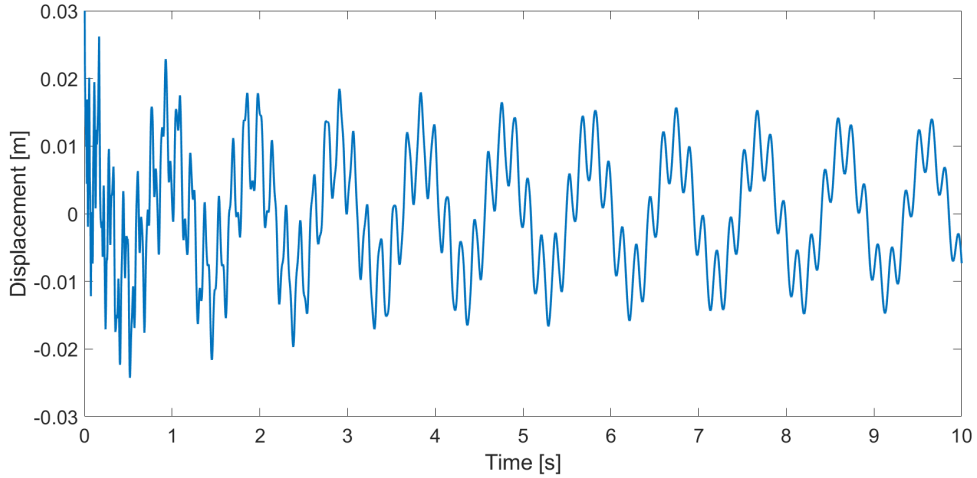

Figure 3.14: Simulation of tip of the boom when subject to initial displacement

	Natural frequency [Hz]		
Bending mode	Analytical	Frequency domain	Time domain
1	1.0	1.0	1.0
2	6.5	6.5	6.5
3	18.3	18.3	

Table 3.3: Numerically obtained natural frequencies of the boom corresponding to the first three bending modes when solving the model in the frequency domain

Table 3.3 shows that the natural frequencies determined in the frequency and time domain correspond with the analytically derived natural frequencies. Thus, the model of the boom includes the right frequencies.

3.4.3. Load

The verification of the load is performed by comparing the displacement and frequency of the load of a time simulation to analytically derived frequency and displacement.

The frequency is calculated by assuming a single pendulum and is calculated according to (2.17). The theoretical maximum displacement is calculated by assuming that all the kinetic energy is transformed into potential energy. This can be calculated using:

$$\frac{1}{2}M_l\dot{y_b}^2 = M_l g\Delta h = M_l g L_{wr}(1 - cos(\beta_1)) \tag{3.28}$$

This can only be used if the duration of acceleration is significantly smaller than the natural period of the load. In this equation $\dot{y_b}$ represents the horizontal velocity of the top of the wire rope. This equation is rewritten to obtain the angle β_1, which is given by:

$$\beta_1 = cos^{-1}\left(1 - \frac{\dot{y_b}^2}{2gL_{wr}}\right) \tag{3.29}$$

The time simulation accelerates the load in 1 second from 0 to $1.75\ m/s$. In addition, the length of the wire rope is set to 60 metres. Thus the maximum theoretical displacement is $4.1°$ and the period of oscillation should be 15.5 seconds. The results of the time simulation is shown in Figure 3.15. Here, the blue line represents β_1 and the red line β_2. The two dashed black lines show the limit when the load is modelled as a single pendulum. This figure shows that the displacement comes close to the theoretical value, which is expected because the duration of the acceleration is much smaller than the natural period of the load. In addition, the swinging period, which is 15.7 seconds, corresponds to the natural period. The second angle β_2 oscillates around β_1 as would be expected. Thus, the model of the load responds according to the expectations.

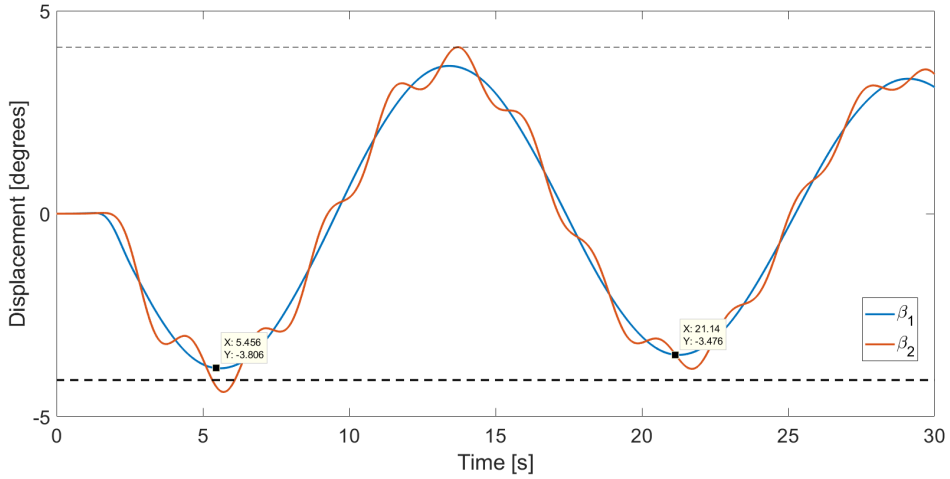

Figure 3.15: Displacement of the load subject to acceleration from 0 to 1.75 m/s in 1 second

3.5. Controller

The following components of the controller should be included in the model according to section 2.10:

- PI-controller
- Ramp function
- Play compensation

Figure 3.16 shows the simplified motor control scheme implemented in MATLAB to control the two motor groups. This scheme shows that the desired speed goes through the ramp function to create a s-curve. The actual speed of both motor groups is subtracted from the s-curve to create the speed error, which is the input for the PI-controller. The PI-controller determines the required torque from the speed error. The torque from both motor groups is averaged and the torque offset determines the torque that is subtracted from one group and added to the other group to compensate the play. Essentially, the play compensation maps the torque that is sent to the motor groups according to Appendix B. Thus, the torque determined by the PI-controller plus or minus the torque offset is the input torque that is applied on the two motor groups.

In MATLAB, the play compensation was initially switched off to check whether the PI-controller determines the correct torque such that the motors follow the s-curve. Figure 3.17 shows in red the s-curve and in blue the simulated response of one of the motor groups. This shows that the response follows the s-curve well, but with some delay. This delay is expected, because the PI-controller only calculates a torque when there is a speed error.

The next step is to switch on the play compensation, while including an external force that represents the swinging motion of the load. Figure 3.18 shows the torque delivered by both motor groups and the average torque when the crane accelerates from 5 to 9.4 seconds. Here, the black line is the average torque and the blue and red line represent the torque delivered by group 1 and 2, respectively. The vertical axis represents the torque delivered by the motors as a percentage of the rated nominal torque,

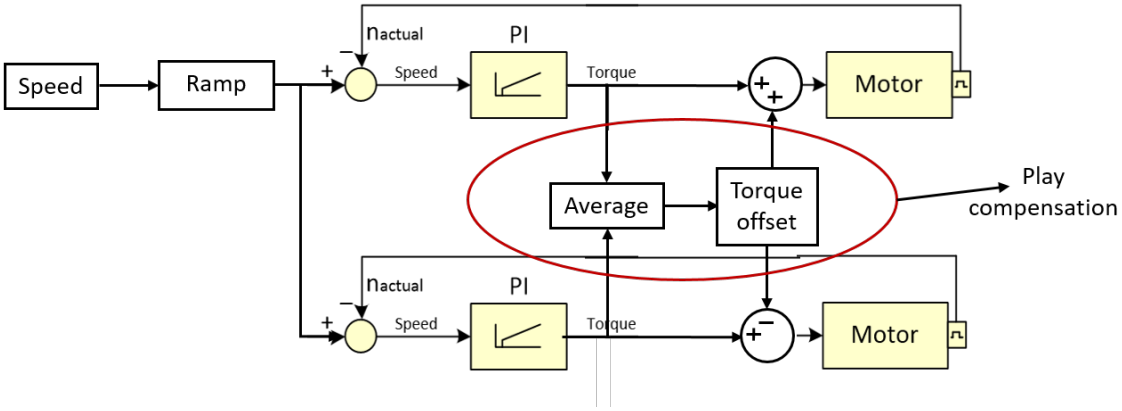

Figure 3.16: Simplified control scheme as implemented in MATLAB

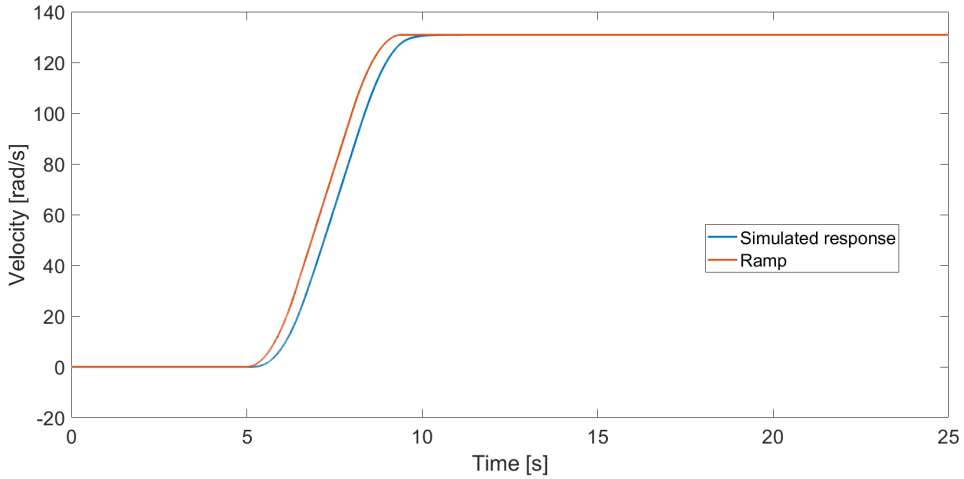

Figure 3.17: Velocity of crane (blue) when controlled by PI-controller including ramping function (red)

T_{100}. During the first two seconds, the gears are being put under tension and after 2 seconds, the play is pressed out of the system. Five points were taken to see if the groups deliver the torque corresponding to the play compensation as presented in Appendix B. Table 3.4 shows these five points including the average torque required and the torque delivered by group 1, T_1, and group 2, T_2, with their expected values, in percentages of T_{100}. Both motor groups deliver the torque as would be expected from the play compensation.

Time [s]	Average torque [%]	T_1 [%]	$T_{1,exp}$ [%]	T_2 [%]	$T_{2,exp}$ [%]
3.0	0	10	10	-10	-10
6.2	48	92	93	0	3
8.2	57	87	88	24	24
12.4	18	46	46	-10	-10
19.6	-18	10	10	-46	-46

Table 3.4: Five random points taken from the torque in the gearbox with play compensation to check if the two motor groups deliver the torque according to the play compensation

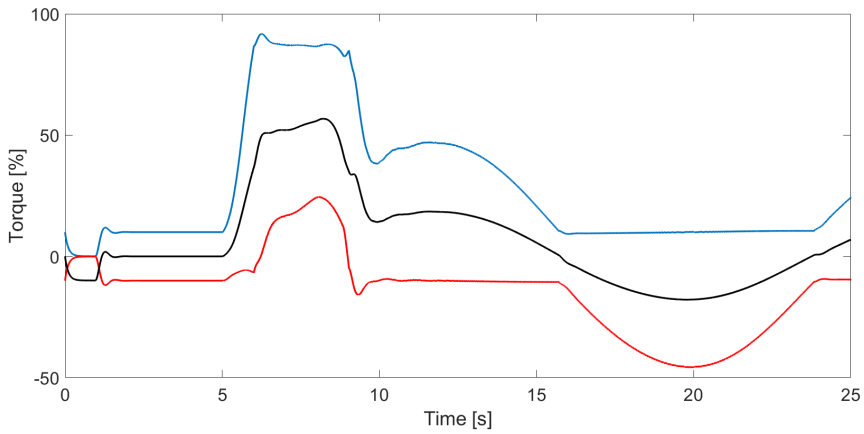

Figure 3.18: Torque required per motor group (black) and torque delivered per group (blue and red)

3.6. Final model

The final model consists of the combination of the three mechanical models and the controller. The method of finite element matrix assembly creates the interaction between the three mechanical models to obtain the set of equations that describe the motion of the whole crane.

Figure 3.19 shows schematically the nodes of the slew drive system and the boom. This figure shows an example of the number of nodes chosen, namely, 2 motor groups are modelled and a boom with 5 nodes. In the model, the number of motor groups modelled and the number of nodes of the boom are parametric. A pivot connects the boom and the crane house. Therefore, the first node of the boom, node 4, can be rewritten in terms of the rotation of the crane house, which is node 3, as explained in section 3.3.2. Figure 3.20 shows the three nodes of the load. The displacement of the 9^{th} node equals to the lateral displacement of the 8^{th} node of the boom, y_5.

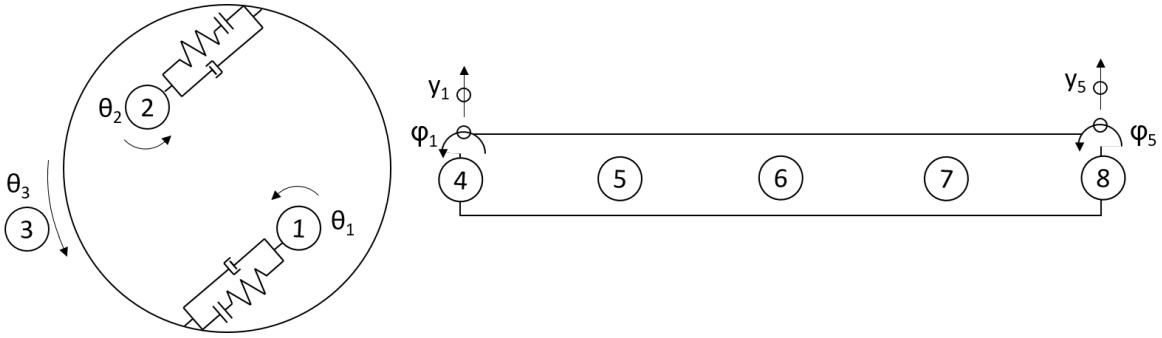

Figure 3.19: Schematic representation from the top with the nodes shown in circles. On the left, the slew drive system is shown and on the right the boom

The matrices of the separate mechanical models are assembled into one large matrix and the elements of the overlapping degrees of freedom can be added together. Figure 3.21 visualises the three separate matrices assembled into one large matrix, with the degrees of freedom on the right. In this figure, the top left in blue represents the matrix of the drive system, the grey area corresponds to the boom and the orange right below is the load. Two degrees over freedom overlap, hence the corresponding elements can be added together and these elements are:

- $D + B$ on location 3x3 in the matrix, which is the interaction between the drive system and the boom, i.e. θ_h
- $B + L$ on location 13x13 in the matrix, which is the interaction between the boom and the load, i.e. y_5

At these places, the elements of the matrices can be added together.

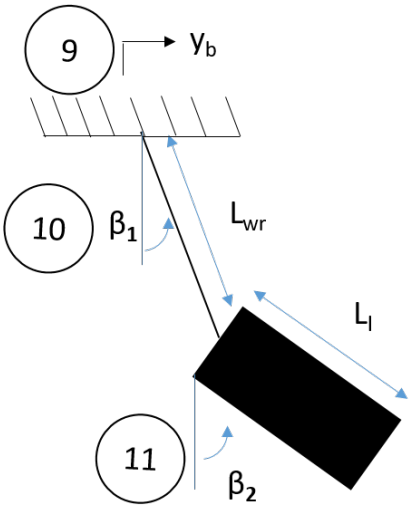

Figure 3.20: Schematic representation of the nodes of the load connected with the boom

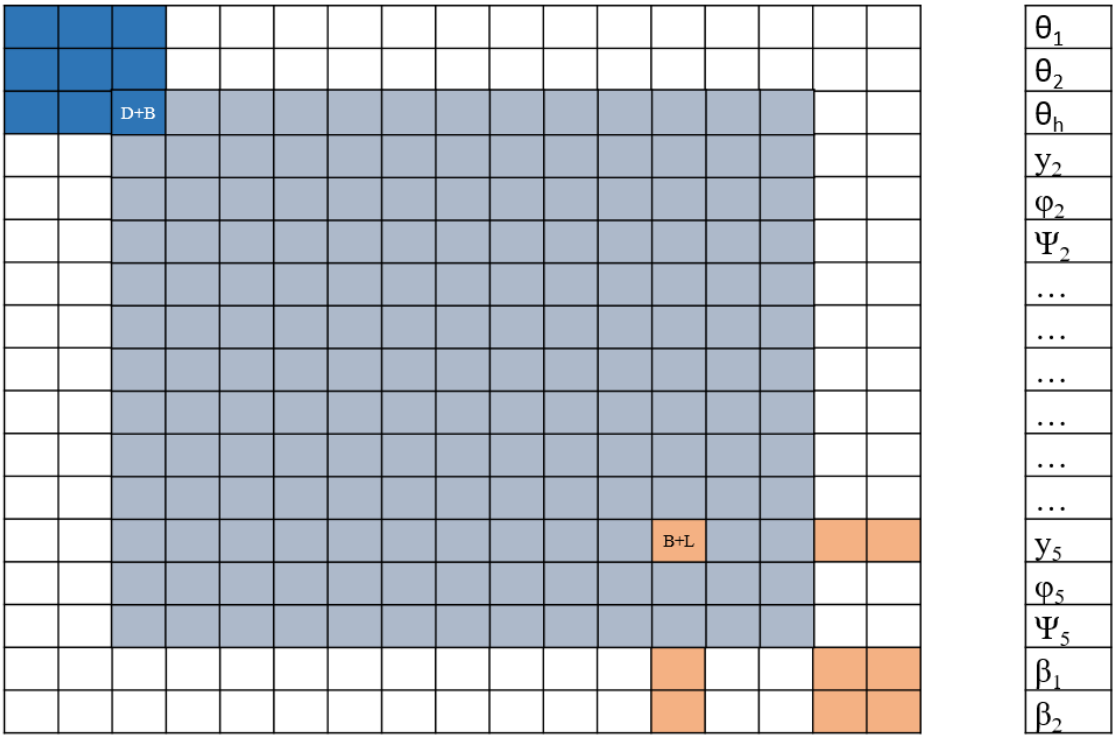

Figure 3.21: Table showing how the three mechanical models are assembled in one matrix. The blue matrix corresponds to the model of the slew drive system, the grey matrix to the boom and the orange matrix to the load. There are two places where the individual matrices overlap, at 3x3 and 13x13

The controller determines the required torque per motor group, which is applied on each of the two motor groups. Appendix C describes shortly the steps taken to implement the model in MATLAB.

Verification

Figure 3.22 shows a time simulation of the final model. This shows the rational velocity of the motors, the crane house and the boom located at the middle and at the tip with the input velocity from the ramp function. The velocity of these components are translated into the rotational frame of the crane. The motors, crane house and boom should follow the same rotational velocity over time, because these components are linked together. Figure 3.22 shows that these components indeed follow the same

path and the input velocity, which means that the kinematic relations are implemented correctly and the velocity is controlled correctly. In addition, this figure shows after 10 seconds a slow oscillation, as a result of the swinging motion of the load.

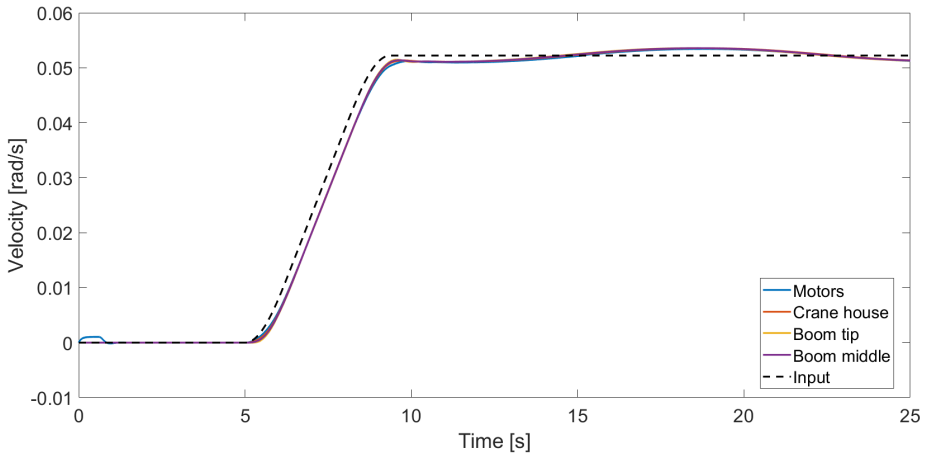

Figure 3.22: Velocity of motors (blue), crane house (red) and boom located at the tip (yellow) and middle (purple) with the input velocity as the dashed black line

Figure 3.23 shows the displacement of the load corresponding to the velocity profile in Figure 3.22. The displacement of the load shows that the velocity is slightly decreases when the displacement of the load is negative. This is expected, because the load exerts a negative force of the crane when its displacement is negative. Thus, the kinematic behaviour on the system is as expected, which means that the final matrices are assembled correctly.

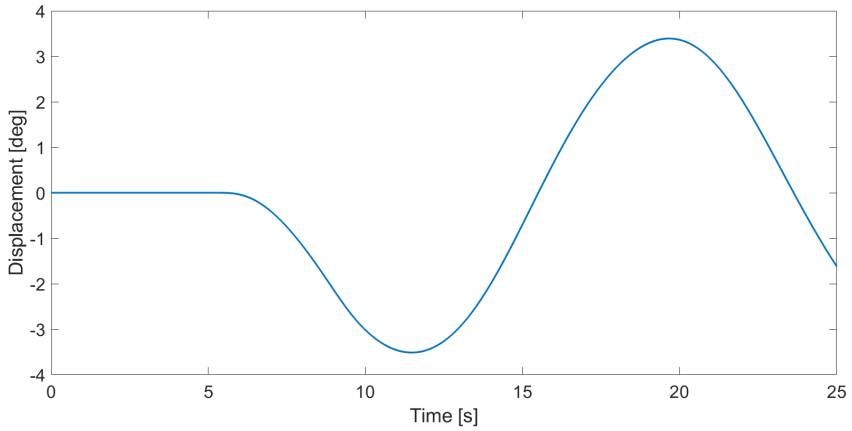

Figure 3.23: Rotational displacement of the load

4

Results

Sections 4.1 and 4.2 investigate the significance of the variable bending stiffness of the boom and how many beam elements are required to sufficiently accurate model the boom, respectively. Section 4.3 compares the model with and without backlash and analyses its influence. Sections 4.4 and 4.5 show the influence of the play compensation and the ramp function, respectively.

4.1. Variable bending stiffness of the boom

The bending stiffness of the boom varies over its length as a result its tapered shape, in reality. The model can be simplified by assuming that the bending stiffness is homogeneous. This influences the natural frequencies of the bending modes, because one equivalent stiffness is chosen instead of a variable bending stiffness. The natural frequencies of the first four bending modes of the boom are determined with boom consisting of 128 beam elements, such that the eigenmodes are determined accurately. Figure 4.1 visualised these four bending modes of the boom. Table 4.1 shows the difference in natural frequencies between a model using varying bending stiffness and one with a homogeneous stiffness. Here, the first column shows the number of bending mode, the second column shows the natural frequency when using the variable bending stiffness. The third column shows the natural frequencies when the boom is simplified as a homogeneous beam while using the bending stiffness corresponding to the average width of the boom. The last column shows the relative deviation between the two models. This table shows that only one natural frequency can be modelled accurately, while the other natural frequencies deviate significantly more than 5%. This means that a homogeneous boom is not sufficiently accurate.

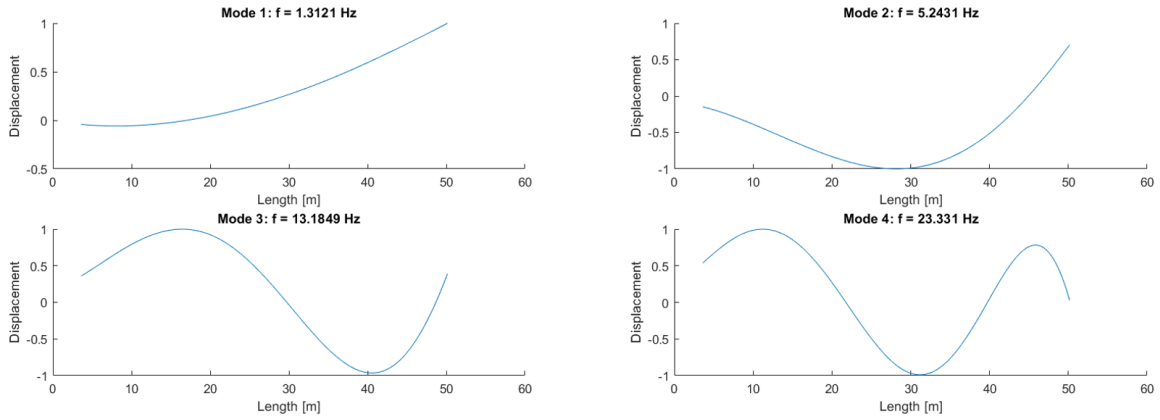

Figure 4.1: First four bending bending modes of the boom while connected to the slew drive system

Mode	Natural frequency variable stiffness [Hz]	Natural frequency constant stiffness [Hz]	Relative deviation [%]
1	1.31	0.99	24.4
2	5.24	4.65	11.3
3	13.2	12.5	5.30
4	23.3	23.3	0

Table 4.1: Natural frequencies of the first four bending modes using of the model with a variable bending stiffness (second column) and comparing this to the model with a constant bending stiffness (third column)

4.2. Number of beam elements

The boom is modelled as multiple beam elements. Increasing the number of elements increases both the accuracy and the computation time. The first and second natural frequency of the lateral bending mode are $1.31\ Hz$ and $5.24\ Hz$ respectively, while the natural frequency of the first torsional mode is $10.4\ Hz$. The frequency of the first torsional mode is already larger than the frequency of the second bending mode. As a result, less torsional eigenmodes will be excited compared to the number of bending modes. The number of beam elements depend on the number of modes that are desired to model. Therefore, the lateral bending modes are dominant in the decision of the number of elements.

The first result aims to find out which bending modes are present in the system. This is done by creating a bode plot, as shown in Figure 4.2. The input of the bode plot is the torque on the motors and the output is the velocity of the boom tip. This figure shows five lines and each line corresponds to a different number of beam elements chosen. Here, it shows that the frequencies corresponding to the first two bending modes of the boom have the largest amplification. In addition, frequencies larger than the frequency of the fifth bending mode, which is $37\ Hz$, have a significantly smaller amplification compared to the amplification of the natural frequency of the first bending mode. Therefore, higher order bending modes than the fifth are not considered in the following results.

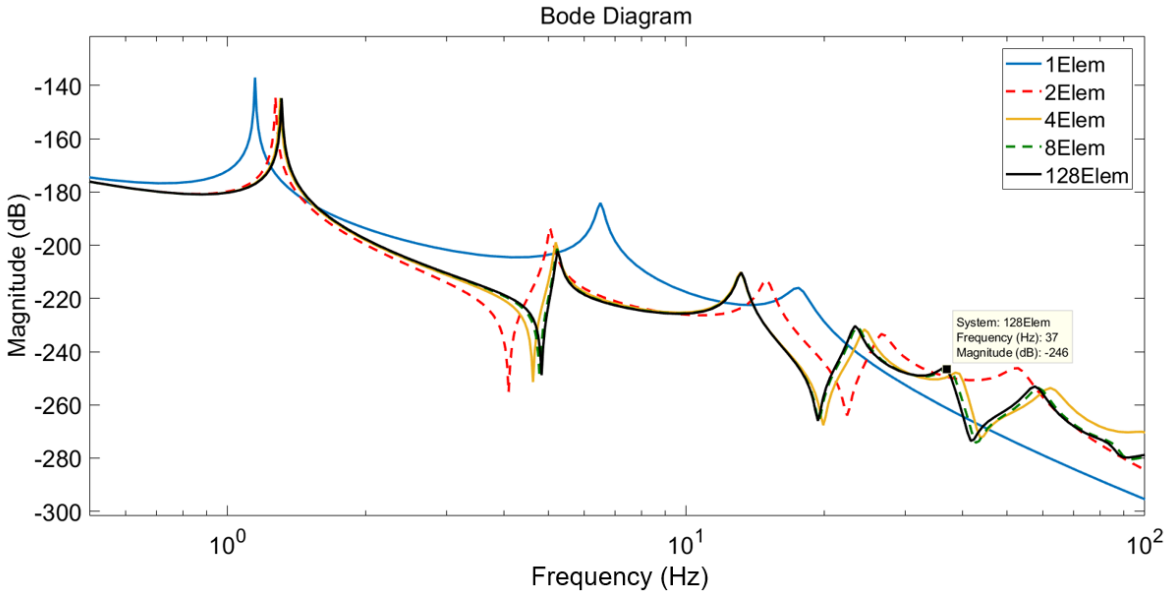

Figure 4.2: Bode plot with input torque on the motors and output velocity of the boom. Bode plot created for five different boom models, each one consists of a different number of elements

The second result shows a convergence study of the natural frequencies corresponding to the first five bending modes, which is shown in Figure 4.3. It shows that 128 elements is well converged, because 32 elements is already converged and it gives an indication of the relative error of the choice of the number of elements.

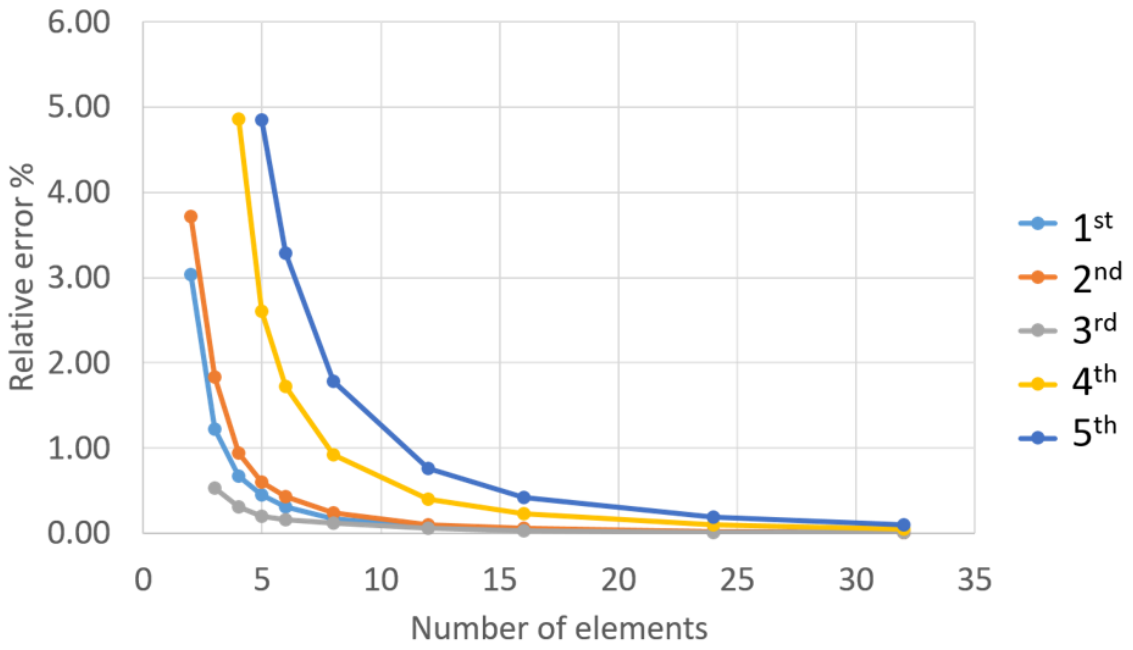

Figure 4.3: Convergence of the natural frequencies for first five bending modes with respect to a 128 element model

The results in the frequency domain cannot capture all the dynamics, like backlash and the influence of the controller. Therefore, the next results consist of time domain simulations. These simulations include the interaction between the controller, slew drive system, boom and load. However, play compensation is excluded, such that the effect of backlash is not clouded. In addition, the simulations are performed with the velocity profile as shown on the left of Figure 4.4 and the corresponding acceleration is shown on the right. This velocity profile consists of accelerating with a s-curve, constant velocity and an engineered emergency stop using a linear ramp. Furthermore, the reference model consists of 16 elements. This is chosen, because Figure 4.3 shows that 16 elements can calculate the natural frequency of the first five bending modes with a relative error of less than 0.5%. In addition, more elements experience numerical problems.

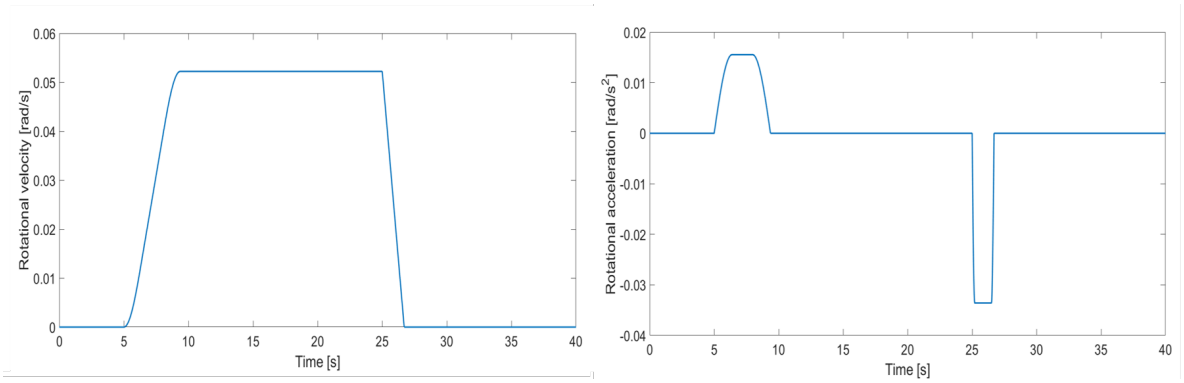

Figure 4.4: Velocity profile (left) used in time simulation and corresponding acceleration (right)

The first result in the time domain is the response of the acceleration of the boom tip, as shown in Figure 4.5. Here different boom models consisting of 1, 2, 3 and 4 beam elements are compared to the model consisting of 16 elements. Models with more than 4 elements are not shown, because these results coincide with the reference model. The acceleration as a result of the velocity profile, given by Figure 4.4, is shown in Figure 4.5. This figure shows firstly that the highest frequency present is 5.4 Hz, which corresponds to the natural frequency of the second bending mode of the boom. When the

crane goes through the play, the crane is subject to a shock load, which should amplify all the natural frequencies present. Figure 4.2 shows that higher frequencies have little amplification. Therefore, it is expected that only the first and second natural frequency are visible when the crane goes through its play. Furthermore, a boom using two elements can already simulate this higher order vibration, because two elements include these frequencies. However, more elements increase the accuracy. Lastly, at five seconds, a small increase in acceleration is visible before the system goes through the play. In reality, this is not expected, because the crane should move once it goes through its play. In the numerical simulation, some damping is required to prevent numerical problems, which results is this small acceleration before the gears go through their play. This increase in acceleration is very small compared to the acceleration after the gears go through their play. Therefore, this simulation can still approximate the reality.

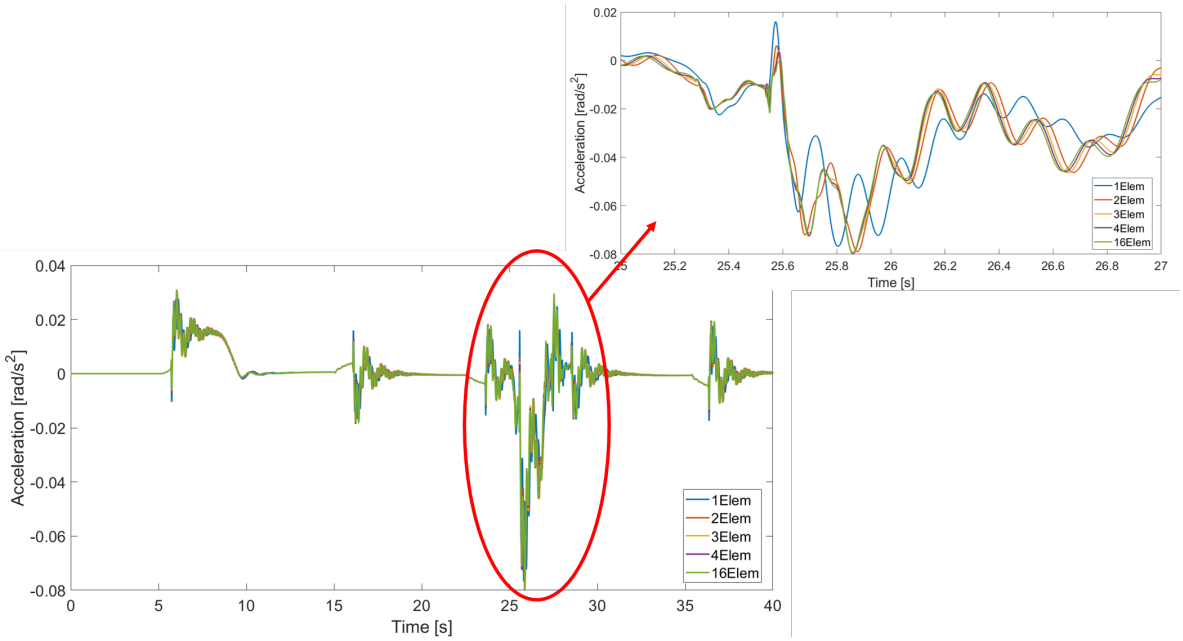

Figure 4.5: Acceleration of the boom tip for five different models containing different number of elements

The second result in the time domain shows a convergence study of the number beam elements required to sufficiently accurate calculate the shear force in the boom. The relative error for this study is calculated as the relative deviation with respect to the reference model, which consists of 16 elements. Figure 4.6 shows the shear force in the boom over its length when subject to the velocity profile given in Figure 4.4 during the emergency brake. The shear force on the left of Figure 4.6 is large, because this force corresponds to the reaction force in the pivot. The pivot accounts for all the reaction force resulting from the boom such that a force equilibrium is achieved, which leads to the pivot experiencing the largest force. In the most right of Figure 4.6, the shear force increases again, as a result of the load exerting an external force on the tip of the boom as a result of its swinging motion. The average shear force over the length of the boom is calculated for different number of elements and is compared to the reference model to perform a convergence study, as shown in Figure 4.7. This figure shows that the model consisting of 16 elements in converged, because the graph converges to zero. In addition, it shows that a relative error of less than 5% is achieved at 3 elements.

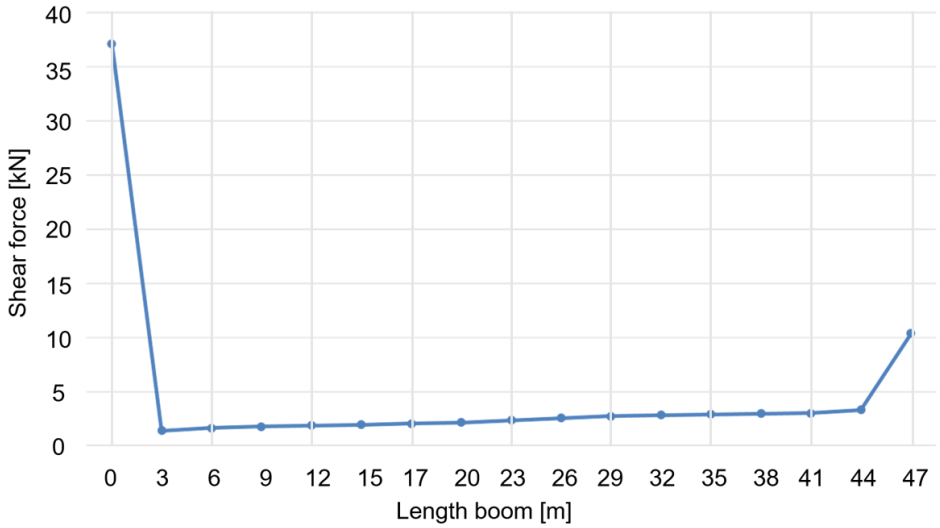

Figure 4.6: Shear force over the length of the boom when modelling the boom using 16 beam elements. Shear force at tip increases as a result of the swinging motion of the load. The most left point corresponds to the pivot force, which equals to the sum of the shear force over the length of the boom

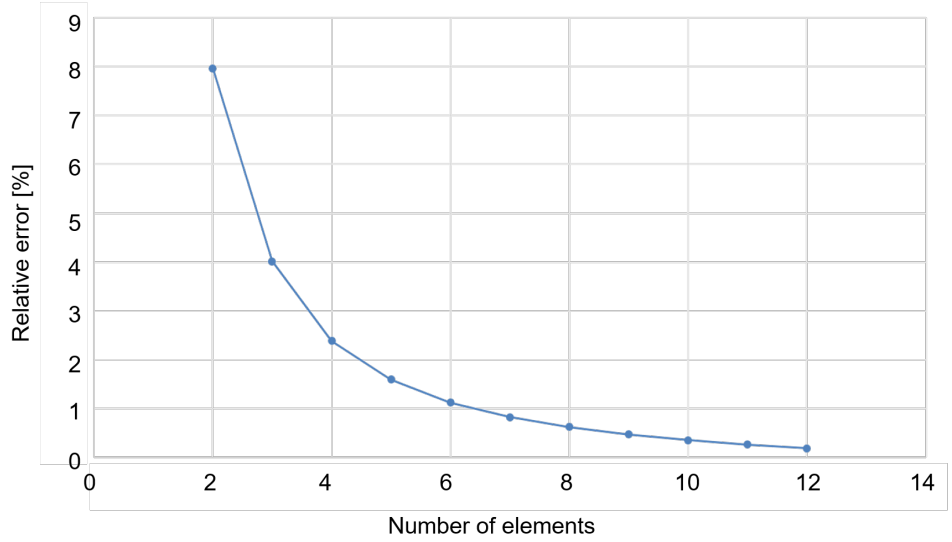

Figure 4.7: Convergence study of the average shear force over the length of the boom during maximum shear force

The choice regarding the number of elements is always a compromise between simulation time and accuracy. Figure 4.8 shows the simulation time as a function of the number of elements corresponding to the velocity profile used. The simulation time shows an exponential increase when the number of elements rise. Figure 4.9 shows the multiplication of the relative error and the simulation time. This figure shows that the first part is dominated by the decrease in relative error and the second part is dominated by the increase in simulation time. It also shows that the multiplication of the relative error and simulation time is smallest for 5 and 6 elements. Using 6 elements has the same order of magnitude of simulation time as 5 elements, while 6 is more accurate. Therefore, the choice is made to model the boom using 6 elements, which is also used in the following sections.

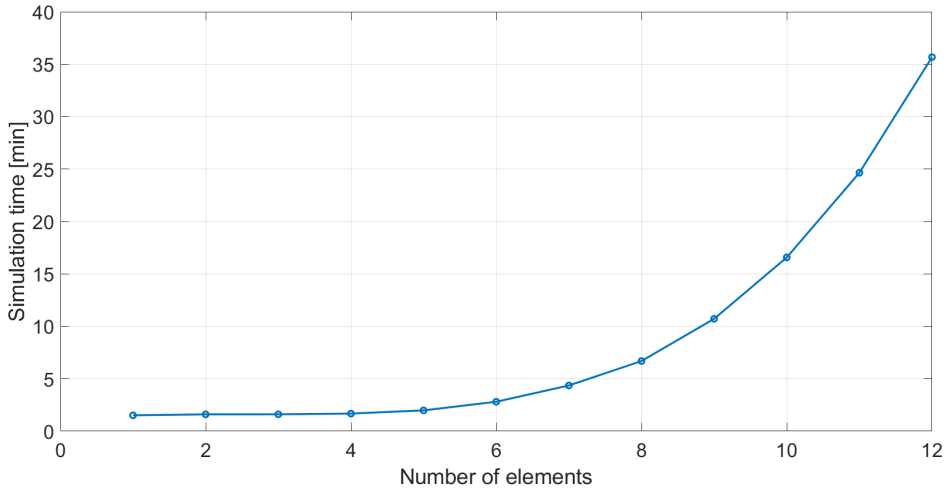

Figure 4.8: Simulation time as a function of the number of beam elements

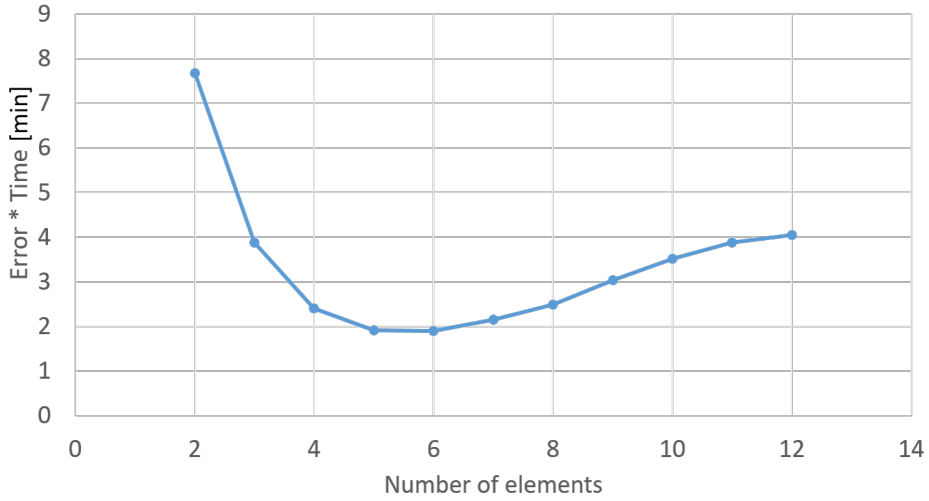

Figure 4.9: Multiplication of simulation time and the relative error as a function of the number of elements

4.3. Comparison with and without backlash

The red and blue lines in the figures in this section represent the response with and without backlash, respectively. The simulations in this section only exclude play compensation, because this would cloud the consequences of backlash.

Figure 4.10 shows the acceleration input time signal and Figure 4.11 shows the response of the acceleration of the boom tip with and without backlash. This figure shows that suddenly vibrations occur with backlash, when the torque in the gearboxes change sign, which means that they go through their play. This results in a shock load to the system, which excites the natural frequencies of the system.

Figure 4.12 shows the torque in the gearboxes and the rotation of the load in a double y-axis plot. The left axis represents the torque in the gearboxes and the right axis represents the rotation of the load. The torque in the gearboxes first shows an increase as a result of the acceleration of the crane. A slow oscillation is visible during constant velocity, which corresponds to the rotation of the load as represented by the dashed black line. This figure shows the moment that the torque in the gearboxes change sign, which is the moment that backlash occurs. In this simulation, the gearboxes change sign as a results of rotation of the load and the acceleration of the crane.

Figure 4.11 shows that the vibration, when backlash is included, consists of two frequencies during

acceleration, namely 1.3 and 5.2 Hz, which correspond to the first and second natural frequency of the boom, respectively. In comparison, this figure shows that during braking, a low frequent vibration occurs without backlash, which corresponds to the first natural frequency, 1.3 Hz. This vibration is a result of the large jerk on the system from the sudden change in acceleration during braking. These figures show that the frequencies of vibration correspond to the natural frequencies of the boom. This means that these vibrations would not occur if the boom is modelled rigidly or by only a beam model that can determine the first lateral bending mode of the boom. The pedestal crane on the Sleipnir showed the same two frequencies when it vibrates, as shown in Figure 4.11 with backlash. These are a lower frequent vibration in the order of 1 Hz and a more high frequent vibration in the order of 5 Hz. Therefore, backlash in combination with a flexible boom is required to model the higher order vibrations. In addition, this model has the ability to predict the same vibrations as were visible in the pedestal crane on the Sleipnir during the design phase.

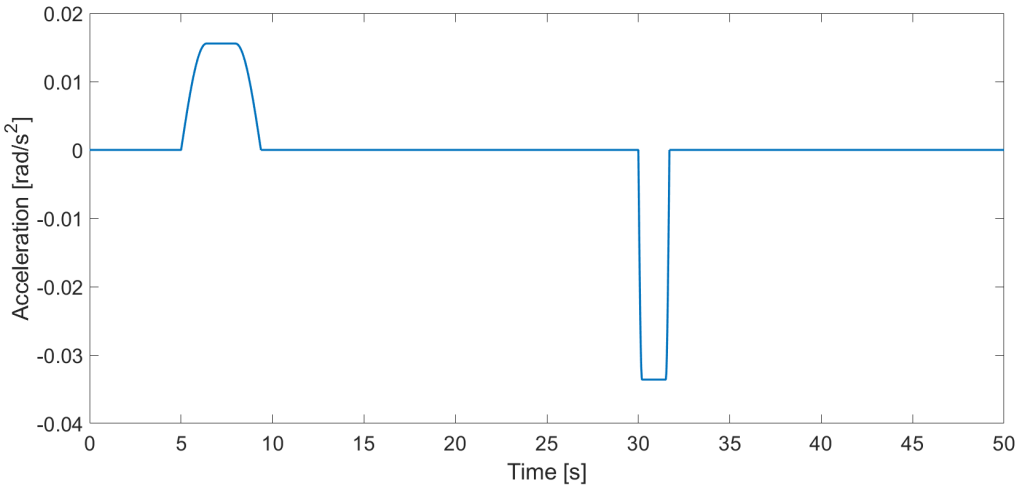

Figure 4.10: Acceleration profile in the rotational frame of the crane, which is used a input

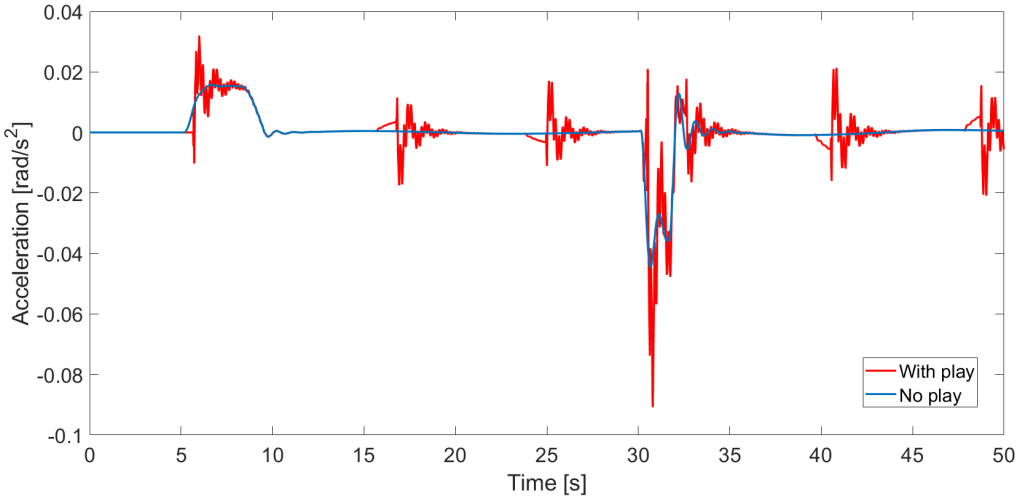

Figure 4.11: Acceleration response of the boom tip with backlash (red) and without backlash (blue)

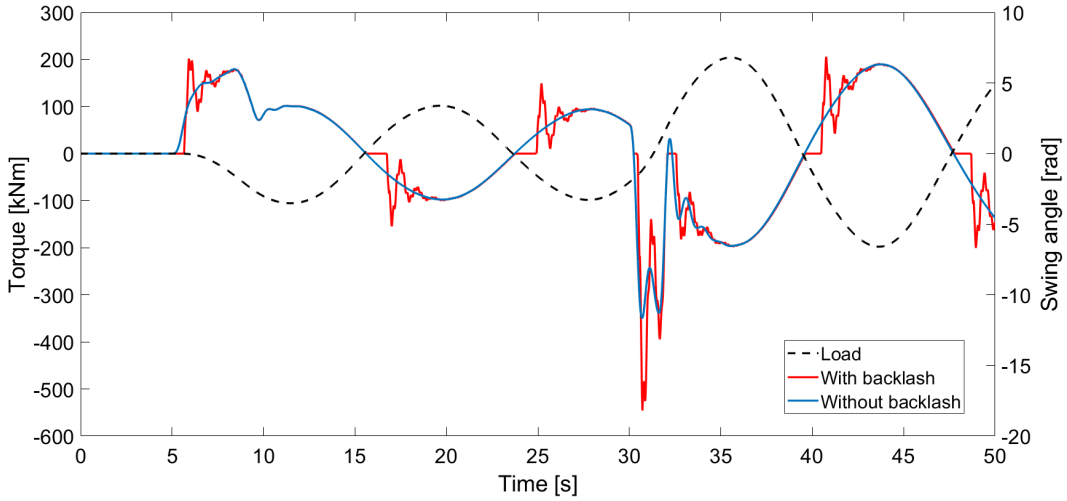

Figure 4.12: The left y-axis shows the torque in the gearboxes with backlash (red) and without backlash (blue). The right axis shows the corresponding sidelead angle of the load, the black dashed line represents this

Figure 4.13 shows the response of the acceleration of the crane house as a result of the time signal shown in Figure 4.10. The acceleration of the crane house shows many frequencies the moment the gears go through their play, the high frequent vibrations damp out quickly and a vibration with a frequency of $5.2\ Hz$ remains in the system the longest. This corresponds to the high order vibration, which is also present in the boom as shown in Figure 4.11. The amplitude of the vibrations in the crane house is larger than in the boom and the vibrations damp out less quickly than in the boom. This can be explained by the fact that the shock load as a result of backlash acts directly on the crane house. While the boom has some stiffness through which the shock load travels. Stiffness acts like a low pass filter, causing the vibrations to be less severe. In addition, the boom has an additional damping term as a result of material damping. The combination of the stiffness of the boom and the damping term leads to the boom experiencing less severe vibrations than the crane house. Thus, the vibrations are most severe in the crane house. The crane cabin for the operator is assembled on the crane house. Therefore, it is important to consider the frequencies of the vibrations in the crane house for the design of the cabin to ensure the safety of the operator.

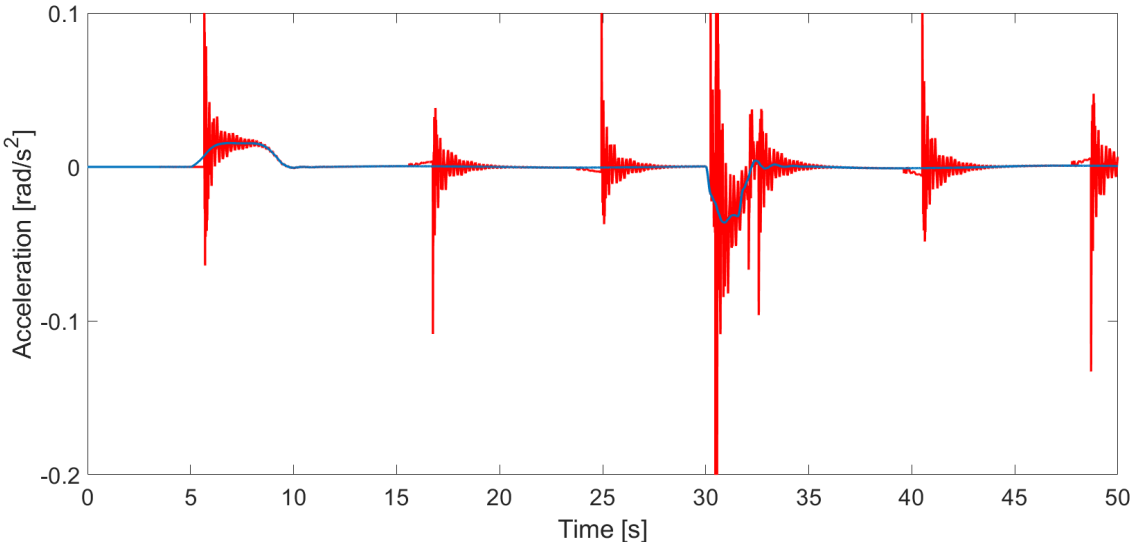

Figure 4.13: Acceleration of the crane house with backlash (red) and without backlash (blue)

Figure 4.14 shows the slewing moment corresponding to the acceleration response shown in Figure 4.11. In addition, this figure shows with the dashed black line the slewing moment determined by the current quasi static models, which is calculated with:

$$M_{slew} = J_b\ddot{\theta}_h + M_l g L_{wr} sin(\beta_{sidelead}) \tag{4.1}$$

Here, $\beta_{sidelead}$ is the sidelead angle given by the specifications of the crane and $\ddot{\theta}_h$ represent the input acceleration of the crane during either accelerating or braking and the heel is set equal to $0°$. The numerical values corresponding to this equation are given in Table 4.2. The black dashed line, in Figure 4.14, shows that during acceleration and constant velocity, the slewing moment is larger when calculated with (4.1) than the results from the simulation. The quasi static model assumes one constant sidelead angle, while this angle changes over time during the simulation. As a result, the maximum sidelead of the numerical simulation during acceleration and constant velocity is $3.3°$, as shown in Figure 4.12, which is lower than the sidelead angle resulting in a lower slewing moment. However, during braking, the slewing moment with backlash becomes larger than determined by the quasi static model, as a result of a larger rotation angle of the load and the amplitude of the shock load. In addition, the quasi static model cannot capture the vibrations that occur as a result of backlash and the flexibility of the system, while this is possible with the dynamical model.

Parameter	Numerical value
J_b	$5.4 \cdot 10^7\ kgm^2$
$\ddot{\theta}_{h,accelerating}$	$0.0156\ rad/s^2$
$\ddot{\theta}_{h,braking}$	$0.0336\ rad/s^2$
M_l	$30 \cdot 10^3\ kg$
g	$9.81\ m/s^2$
L_{wr}	$60\ m$
$\beta_{sidelead}$	$5°$

Table 4.2: Numerical data to determine the slewing moment of the quasi static model currently used

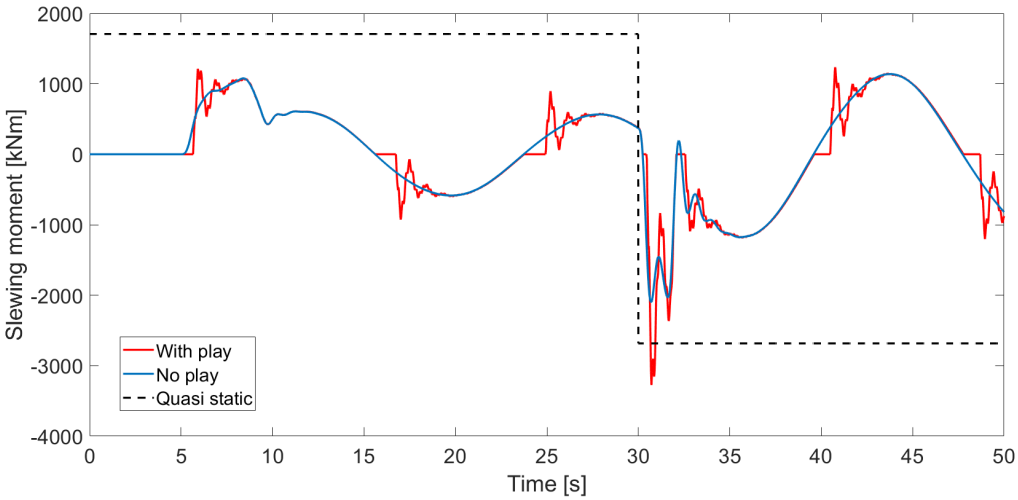

Figure 4.14: Slewing moment determined by the dynamical model with backlash (red) and without backlash (blue) and determined by the quasi static model represented by the dashed black line

4.4. Comparison with and without play compensation

Huisman implemented a control function to compensate the play. In this section, the blue and red lines in the figures correspond to the model with and without play compensation, respectively.

Figure 4.15 shows the acceleration of the boom tip with and without play compensation. This figure shows that no vibrations occur until 30 seconds when the play compensation is included. While, vibra-

tions do occur when there is no play compensation. Figure 4.16 shows the torque in the gearboxes for the two motor groups. This figure shows that with play compensation, the gearboxes do no change sign until 30 seconds. While, without play compensation, the gearboxes already changed sign a few times. This figure shows that the play compensation works well to prevent vibrations as long as the motors have enough capacity to deliver a counter acting torque. The moment that the motors do not have enough capacity, the crane goes through its play and starts to vibrate. In this simulation, the only moment that the motors do not have enough capacity to compensate the play is during the emergency brake, which means that this is the only moment that the gears go through their play. The heel of the crane during this simulation is $0°$. In case, the crane is at its maximum heel and the sidelead is maximum, the capacity of the motors during acceleration might not be sufficient to compensate the play, which results in backlash and vibrations. The downside of the play compensation is that is average torque in the gearboxes and motor is larger, which means that these components need to be larger than required without play compensation. Figures 4.15 and 4.16 show that this dynamical model can predict during the design phase the scenarios when play compensation works well and when is does not work well.

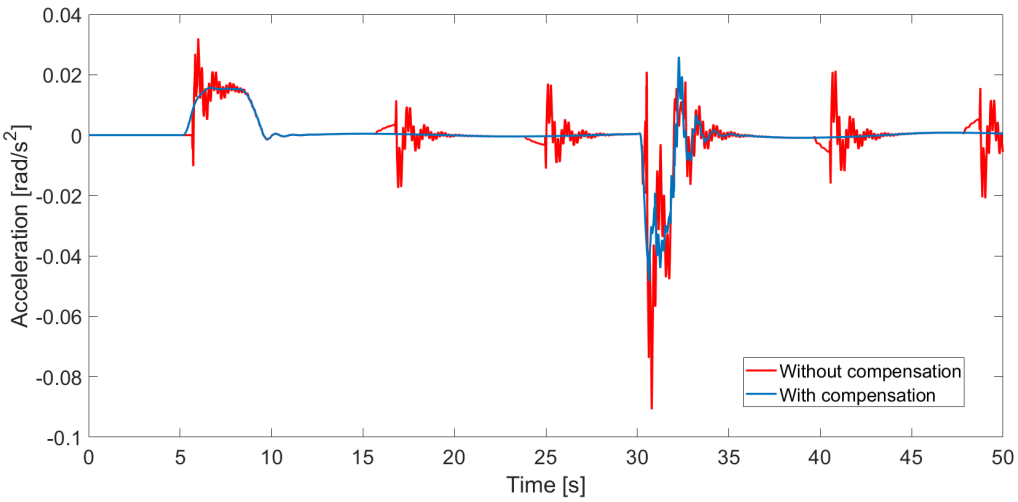

Figure 4.15: Acceleration response of the boom tip with play compensation (blue) and without play compensation (red)

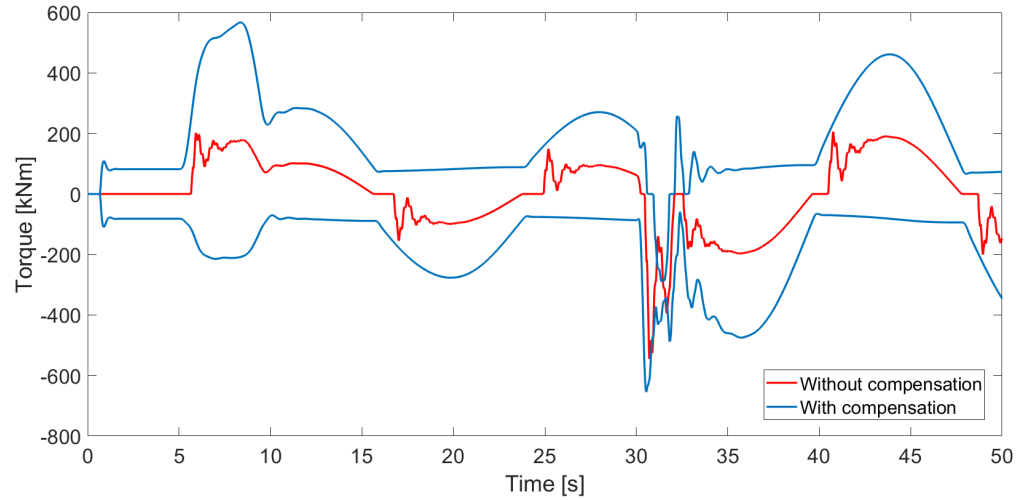

Figure 4.16: Torque in the gearboxes in blue with play compensation and in red without. One blue line corresponds to one equivalent gearbox corresponding to one motor groups and the other corresponds to the equivalent gearbox of the other motor group

4.5. Ramp function

The previous sections used a smooth s-curve. During the design phase, the shape of the s-curve is generally created for the maximum velocity. For lower velocities, the duration of acceleration scales down, e.g. half of the maximum speed means half of the duration of acceleration. The moment that the duration of acceleration shortens, the curved parts of the s-curve shorten. This means that the velocity tends to move to a linear ramp instead of a s-curve for low velocities.

Figure 4.17 shows the input velocity and acceleration on the left and right, respectively, and Figure 4.18 shows the response of the boom tip when subject to this input, with the play compensation. This figure shows that a linear ramp causes vibrations during acceleration, while the s-curve does not show these vibrations. When the velocity profile is a linear ramp, the jerk goes to infinity at the start and end of acceleration. When the boom is subject to an infinite jerk, it tries to instantly change its acceleration, which is not possible in reality. As a result of a large jerk, the boom starts to vibrate, which is visible in Figure 4.18. This figure also shows that this model can predict whether the response of the crane follows the input velocity profile smoothly with the applied s-curve and play compensation.

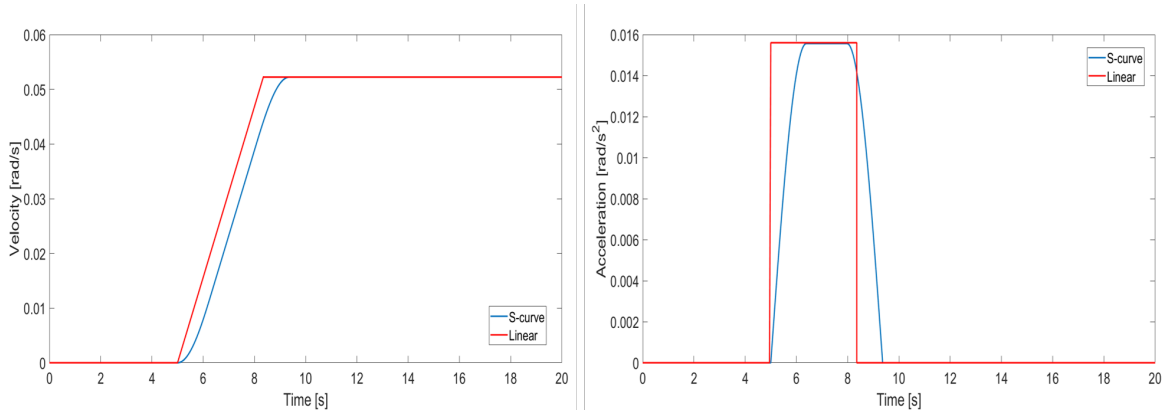

Figure 4.17: On left the velocity profile with a linear ramp (red) and s-curve (blue). On the right, the corresponding acceleration is shown

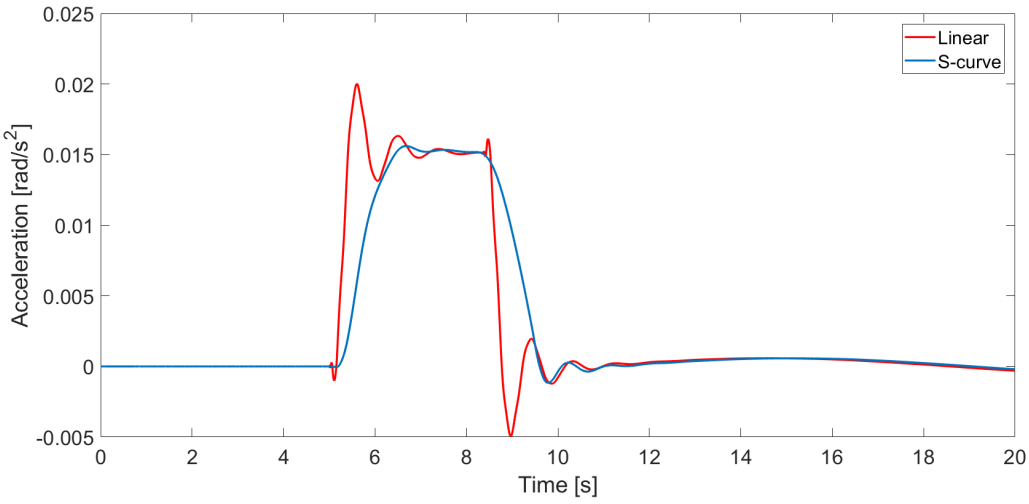

Figure 4.18: Acceleration response of the boom tip with a linear ramp (red) and with a s-curve (blue) with the play compensation being switched on

5

Conclusion

The objective of this master thesis is to create a method to predict the occurring vibrations during slewing during the design phase of a pedestal crane. The occurring vibrations consist of a low and high frequent vibration, which are in the order of 1 and $5\ Hz$, respectively. To be able to predict the occurring vibrations during slewing, a dynamical model of an electrically driven pedestal crane with a lattice boom structure is created that includes the significant dynamics that arise during the slewing motion.

Chapter 2 performed a system analysis, from which can be concluded that the following dynamic effects should be included in the dynamical model to model the dynamics of the slew drive system sufficiently accurate:

- Controller
  - PI-controller
  - Play compensation
  - Ramp function
- Slew drive system
  - Inertia of the motor, gearbox and brake
  - Average mesh stiffness of the gearbox
  - Play in the gearbox and pinion
- Boom
  - Minimum of first two lateral bending modes
  - Variable bending stiffness over its length
  - Torsion
- Load
  - Sidelead
  - Double pendulum behaviour

The mesh stiffness of the gearbox remains significant as long as it result in an additional natural frequency in the order of magnitude of the boom or lower.

Furthermore, the dynamical model is sufficiently accurate by modelling the slew drive system as two equivalent rotating masses. Each mass represents one motor group, which consists of half of the motor, gearbox and brake assemblies. This means that the motors, gearboxes and brakes in one motor group are merged into one equivalent degree of freedom. In addition, the stiffness of the gearbox is included via a spring. The play in the gearbox and pinion is included in this spring. In addition, the boom can be modelled sufficiently accurate with a minimum of 3 beam elements. However, 6 elements

increases the accuracy significantly, while maintaining the same order of magnitude of simulation time. Therefore, 6 elements is a good compromise between accuracy and simulation time. Each element consists of lateral bending and torsion. In addition, the bending stiffness varies per element. A double pendulum describes the motion of the load.

Section 4.3 compared the dynamical model with and without backlash. This comparison showed that a model without backlash cannot excite the higher order natural frequencies of the boom. In addition, backlash can only excite these frequencies if the boom is modelled using multiple beam elements. Thus, the interaction between backlash and the boom model consisting of multiple beam elements is required to be able to predict the occurring vibrations.

Section 4.4 investigated the influence of the play compensation. This section showed that this control function works well, because it significantly reduces the number of times the crane goes through its play. It works well as long as the motors have enough capacity to deliver a counteracting torque. There are scenarios where the capacity of the motors might not be sufficient, e.g. when slewing up the slope as a result of the heel of the crane. When the capacity is insufficient, the crane still goes through its play, which results in vibrations. In addition, the average torque in the gearboxes and power delivered by the motors is higher as a result of the play compensation. The model created during this research can be used to find the ranges in which the play compensation works well. In addition, different shapes of play compensation can be used to test their influence.

Section 4.5 compared a linear ramp and a s-curve. This showed that a linear ramp results in the low frequent vibrations as a result of an infinite jerk. While, a smooth s-curve does not show these vibrations. However, a s-curve takes longer to reach the desired velocity than a linear ramp. The dynamical model created in this thesis can be used during the design phase to test whether crane follows the ramp function smoothly.

To conclude, the model proposed in this thesis can be used during the design phase of a crane to predict the occurring vibrations during the slewing motion. Furthermore, the control functions can be tested to find their influence on the structure.

5.1. Future work and recommendations

The first recommendation is to validate the dynamical model of this thesis with experimental data, which can be done by obtaining experimental data from an electrically driven pedestal crane. The frequency of vibration is important to validate when the crane goes through its play, because this shows the dominant natural frequencies. This can be tested by switching off the play compensation and rotate the crane slowly until it goes through its play, which should amplify the natural frequencies in the system. Accelerometers should be placed on four locations, namely, on the tip, middle and pivot connection of the boom and one on the crane house. These accelerometers should measure the acceleration in the lateral direction of the boom. During this research, it was found that the the natural frequency of the second lateral bending mode of the boom is the highest frequency present. Therefore, the minimum frequency that the accelerometer needs to measure is $5\ Hz$. However, in reality, it is possible that the vibrations consist of higher frequencies. Therefore, the accelerometer should be able to measure a minimum frequency of $25\ Hz$ to have ample margin for unexpected higher frequent vibrations. A Fourier transform of the data from the accelerometer should show the natural frequencies present. A few static parameters should also be tested, to be able to use the same parameters in the dynamical model as the experimental data will show. These are the following parameters:

- Stiffness of the gearbox
- Play of the gearbox and between the pinion the slewing gear
- Bending stiffness of the boom

After validating the natural frequencies, a time signal should be measured. A typical time signal would be to slew $90°$ to one side and slewing back to the start position. The acceleration over time measured by the accelerometers can be compared to the simulated acceleration of the crane to validate the time signal.

The results showed that backlash in combination with the flexibility of the boom results in the occurring vibrations. Therefore, it would be beneficial to eliminate backlash. Play compensation showed that this reduces the number of times backlash occurs significantly. However, it does not eliminate

backlash. In addition, the design with play compensation requires larger motors and stronger gearboxes compared to a design without play compensation. A method to eliminate backlash is to change the gears is the system. Possibilities for gears without backlash are helical gears, herringbone gears or anti backlash (spur) gears.

The control can be optimised by further analysing the ramp function. An idea to improve the ramp function is to play with the backlash by going through the play twice on purpose with a duration between them equal to half of the natural period of the boom. Hence, creating two frequencies out of phase, which will cancel each other. A practical downside of this idea is that the natural period of the boom needs to be known accurately. Otherwise, it is possible that the response can be excited twice.

The results showed that the proposed dynamical model is able to predict vibrations during slewing in a pedestal mounted offshore crane with a rectangular lattice boom structure. Huisman builds and designs more types of cranes and boom configurations. Therefore, this model could be extended by creating boom models for a double lattice structure, box girder and double box girder. Furthermore, research can be performed regarding the difference between the pedestal crane and the other crane types to find which dynamics should be added and which can be neglected with respect to the dynamical model of the pedestal crane. Furthermore, the dynamical model can be extended by including the other motions of the crane, namely hoisting, boom hoisting and in some cases travelling.

Bibliography

[1] World record: Heerema's crane vessel sleipnir lifts 15,300 tonnes, Sep 2019. URL https://hmc.heerema.com/news-media/news/world-record-heeremas-crane-vessel-sleipnir-lifts-15300-tonnes/.

[2] D. Blackburn, J. Lawrence, J. Danielson, W. Singhose, T. Kamoi, and A. Taura. Radial-motion assisted command shapers for nonlinear tower crane rotational slewing. *Control Engineering Practice*, 18(5):523–531, 2010.

[3] I Chowdhury and P. Dasgupta. Computation of rayleigh damping coefficients for large systems. *Indian Institute of Technology*.

[4] S. Chwastek. Optimization of crane mechanisms to reduce vibration. *Automation in Construction*, 119, 2020.

[5] Donald T Greenwood. *Advanced dynamics*. Cambridge University Press, 2003.

[6] M. K. Gupta, N. Sinha, K. Bansal, and A. K. Singh. Natural frequencies of multiple pendulum systems under free condition. *Archive of Applied Mechanics*, 86(6):1049–1061, 2016.

[7] J. Helsen, F. Vanhollebeke, B. Marrant, D. Vandepitte, and W. Desmet. Multibody modelling of varying complexity for modal behaviour analysis of wind turbine gearboxes. *Renewable Energy*, 36:3098–3113, 2011. doi: 10.1016/j.renene.2011.03.023.

[8] Edgar Matas Hidalgo. Study of optimization for vibration absorbing devices applied on airplane structural elements. *Polytechnic University of Catalonia*, 2014.

[9] J. Huo, H. Wu, W. Sun, Z. Zhang, L. Wang, and J. Dong. Electromechanical coupling dynamics of tbm main drive system. *Nonlinear Dynamics*, 90:2687–2710, 2017. doi: 10.1007/s11071-017-3831-4.

[10] B Jerman. The comparison of the accuracy of two mathematical models, concerning dynamics of the slewing cranes. *FME Transactions*, 34(4):185–192, 2006.

[11] B. Jerman and J. Kramar. A study of the horizontal inertial forces acting on the suspended load of slewing cranes. *International Journal of Mechanical Sciences*, 50(3):490–500, 2008.

[12] B. Jerman, P. Podržaj, and J. Kramar. An investigation of slewing-crane dynamics during slewing motion - development and verification of a mathematical model. *International Journal of Mechanical Sciences*, 46(5):729–750, 2004.

[13] Master Thesis Johan Nugteren. Investigation in the swing motion of a load in an offshore crane. Master's thesis, Delft University of Technology, 3 2020.

[14] A. Labuschagne, N. F. J. van Rensburg, and A. J. van der Merwe. Comparison of linear beam theories. *Mathematical and Computer Modelling*, 49(1-2):20–30, 2009. doi: 10.1016/j.mcm.2008.06.006.

[15] P. A. A. Laura, J. L. Pombo, and E. A. Susemihl. A note on the vibrations of a clamped-free beam with a mass at the free end. *Journal of Sound and Vibration*, 37(2):161–168, 1974. doi: 10.1016/S0022-460X(74)80325-1.

[16] X.H. Li, H.B. Yu, M.Z. Yuan, J. Wang, and Y. Yin. Dynamic modeling and analysis of shield tbm cutterhead driving system. *Journal of Dynamic Systems, Measurement and Control, Transactions of the ASME*, 132:1–14, 2010. doi: 10.1115/1.4000818.

[17] X. Liang, M. J. Zuo, and T. H. Patel. Evaluating the time-varying mesh stiffness of a planetary gear set using the potential energy method. *Journal of Mechanical Engineering Science*, 228(3): 535–547, 2014. doi: 10.1177/0954406213486734.

[18] F. Rauscher and O. Sawodny. An elastic jib model for the slewing control of tower cranes. *IFAC-PapersOnLine*, 50(1):9796–9801, 2017.

[19] W. Sun, H. Ma, X. Song, L. Wang, and X. Ding. Modeling and dynamic analysis of cutterhead driving system in tunnel boring machine. *Shock and Vibration*, 2017, 2017.

[20] J. Valle, D. Fernández, and J. Madrenas. Closed-form equation for natural frequencies of beams under full range of axial loads modeled with a spring-mass system. *International Journal of Mechanical Sciences*, pages 153–154, 2019. doi: 10.1016/j.ijmecsci.2019.02.014.

[21] J. Wang, R. Li, and X. Peng. Survey of nonlinear vibration of gear transmission systems. *Applied Mechanics Reviews*, 56:309–329, 2003. doi: 10.1115/1.1555660.

[22] J. Wei, Q. Sun, W. Sun, X. Ding, W. Tu, and Q. Wang. Load-sharing characteristic of multiple pinions driving in tunneling boring machine. *Chinese Journal of Mechanical Engineering*, 26:532–540, 2013. doi: 10.3901/CJME.2013.03.532.

[23] J. Wei, R. Shu, D. Qin, T. C. Lim, A. Zhang, and F. Meng. Study of synchronization characteristics of a multi-source driving transmission system under an impact load. *International Journal of Precision Engineering and Manufacturing*, 17(9):1157–1174, 2016.

[24] werktuigbouw.nl. *Werktuigbouw Formuleboekje*. Mikrocentrum, 5 edition, 2016.

[25] W. Yang, Z. Zhang, and R. Shen. Modeling of system dynamics of a slewing flexible beam with moving payload pendulum. *Mechanics Research Communications*, 34(3):260–266, 2007.